eScience 2 (2022) 467–485

Contents lists available at ScienceDirect

eScience

journal homepage: www.keaipublishing.com/en/journals/escience

Review

Phase engineering of metal nanocatalysts for electrochemical CO_2 reduction

Yanjie Zhai [a,1], Peng Han [b,1], Qinbai Yun [c], Yiyao Ge [c], Xiao Zhang [a,*], Ye Chen [b,*], Hua Zhang [c,d,e,*]

[a] Department of Mechanical Engineering, The Hong Kong Polytechnic University, Hung Hom, Kowloon, Hong Kong, China
[b] Department of Chemistry, The Chinese University of Hong Kong, Hong Kong, China
[c] Department of Chemistry, City University of Hong Kong, Hong Kong, China
[d] Hong Kong Branch of National Precious Metals Material Engineering Research Center (NPMM), City University of Hong Kong, Hong Kong, China
[e] Shenzhen Research Institute, City University of Hong Kong, Shenzhen 518057, China

HIGHLIGHTS

- Phase engineering of nanomaterials (PEN) emerges as a promising tactic to regulate their electrocatalytic performances.
- Recent development in phase engineering of metal nanocatalysts for electrochemical CO_2 reduction reaction was summarized.
- Challenges and perspectives towards phase engineering of metal nanocatalysts for electrochemical CO_2 reduction were proposed.

GRAPHICAL ABSTRACT

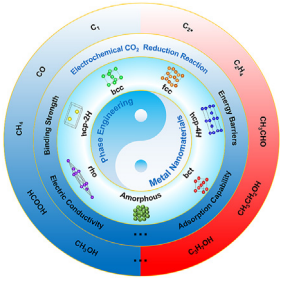

ARTICLE INFO

Keywords:
Phase engineering
CO_2 reduction
Metal nanocatalysts
Electrocatalysis

ABSTRACT

The electrochemical CO_2 reduction reaction (CO_2RR) offers a green and sustainable process to convert CO_2 into valuable chemical stocks and fuels. Metal is one of the most promising types of catalysts to drive an efficient and selective CO_2RR. The catalytic performance of metal nanocatalysts is strongly dependent on their structural features. Recently, phase engineering of nanomaterials (PEN) has emerged as a prominent tactic to regulate the catalytic performance of metal nanocatalysts for the CO_2RR. A broad range of metal nanocatalysts with conventional and unconventional crystal phases has been developed, and remarkable achievements have been made. This review summarizes the most recent developments in phase engineering of metal nanocatalysts for the electrochemical CO_2RR. We first introduce the different crystal phases of metal nanocatalysts used in the CO_2RR and then discuss various synthetic strategies for unconventional phases of metal nanocatalysts. After that, detailed discussions of metal nanocatalysts with conventional and unconventional phases, including amorphous phases, are presented. Finally, the challenges and perspectives in this emerging area are discussed.

1. Introduction

Over the past decades, the rapid consumption of fossil fuels has significantly increased the CO_2 concentration in the atmosphere and caused significant environmental impacts, including global warming and water acidification [1]. Converting CO_2 into value-added chemicals is a promising way to mitigate the drawbacks induced by excessive CO_2 [2]. Recently, with the continuous decrease of renewable electricity prices

* Corresponding authors.
E-mail addresses: xiao1.zhang@polyu.edu.hk (X. Zhang), yechen@cuhk.edu.hk (Y. Chen), hua.zhang@cityu.edu.hk (H. Zhang).
[1] These authors contribute equally.

https://doi.org/10.1016/j.esci.2022.09.002
Received 31 May 2022; Received in revised form 7 August 2022; Accepted 19 September 2022
Available online 24 September 2022

[3], the electrocatalytic CO_2 reduction reaction (CO_2RR) is emerging as a sustainable and economical technology to realize this goal. Compared with conventional chemical processes [4], the electrochemical approach shows excellent advantages, including: 1) ability to use renewable energy input, 2) operation under ambient conditions, 3) clean process with less waste, and 4) ease of equipment set-up and control [5,6]. With the rational design of the electrochemical cell, electrochemical process, and catalyst, CO_2 can be reduced into diverse value-added products, such as carbon monoxide (CO), formate, methane (CH_4), methanol (CH_3OH), ethylene (C_2H_4), ethanol (C_2H_5OH), and n-propanol (C_3H_7OH), thus

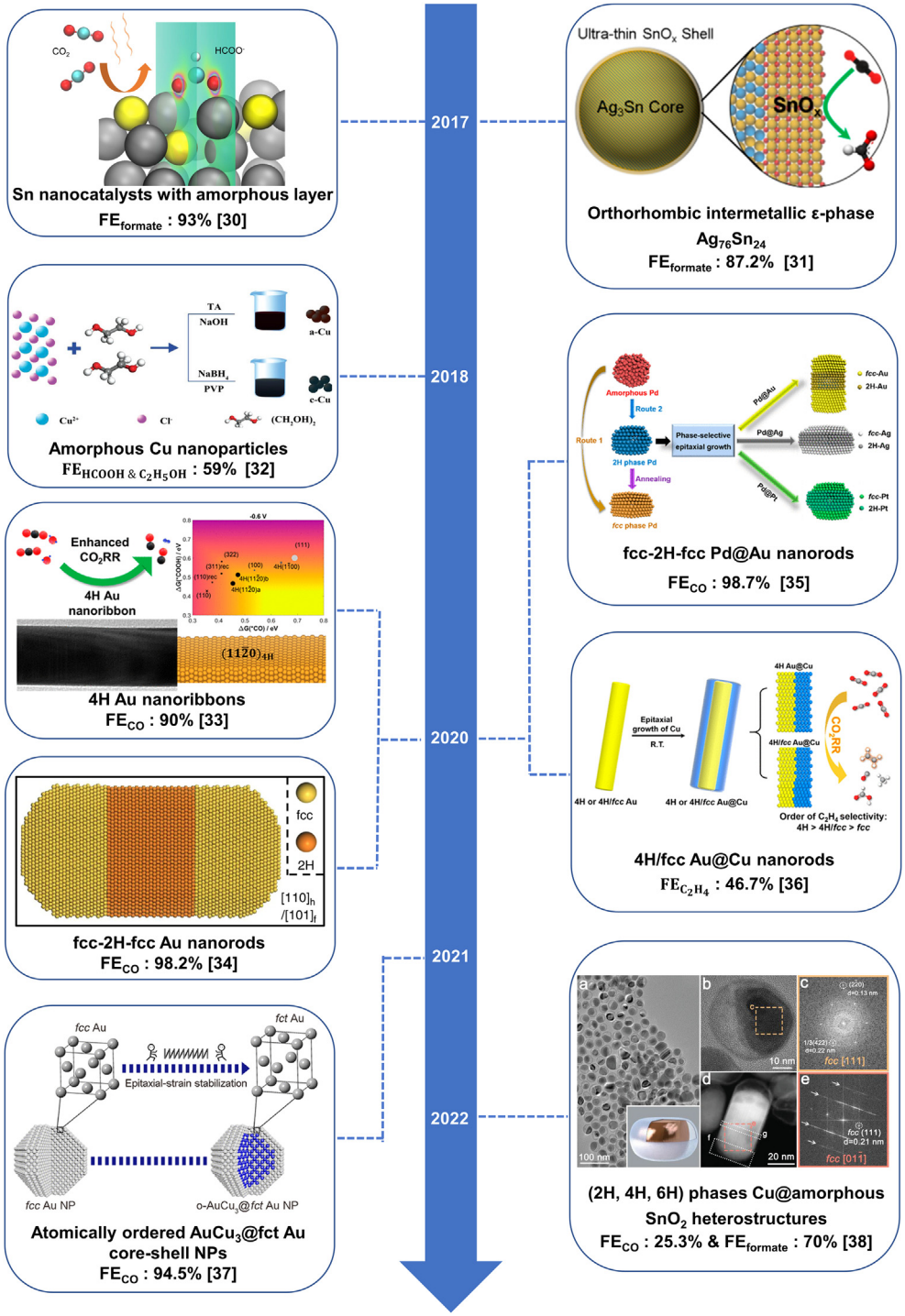

Fig. 1. Timeline of representative works in phase engineering of metal nanocatalysts for the electrochemical CO_2RR in recent years. Sn nanocatalysts with amorphous layer: Reproduced with permission from Ref. [30]. Copyright 2017, Cell Press. Orthorhombic intermetallic ε-phase $Ag_{76}Sn_{24}$: Reproduced with permission from Ref. [31]. Copyright 2017, American Chemical Society. Amorphous Cu nanoparticles: Reproduced with permission from Ref. [32]. Copyright 2018, John Wiley & Sons, Inc. 4H Au nanoribbons: Reproduced with permission from Ref. [33]. Copyright 2020, American Chemical Society. fcc-2H-fcc Au nanorods: Reproduced with permission from Ref. [34]. Copyright 2020, Nature Publishing Group. fcc-2H-fcc Pd@Au nanorods: Reproduced with permission from Ref. [35]. Copyright 2020, American Chemical Society. 4H/fcc Au@Cu nanorods: Reproduced with permission from Ref. [36]. Copyright 2020, American Chemical Society. Atomically ordered $AuCu_3$@fct Au core–shell nanoparticles: Reproduced with permission from Ref. [37]. Copyright 2021, American Chemical Society. (2H, 4H, 6H) phases of Cu@amorphous SnO_2 heterostructures: Reproduced with permission from Ref. [38]. Copyright 2022, John Wiley & Sons, Inc.

making it possible to revolutionize the way these chemicals are produced in the conventional chemical engineering industry.

Electrocatalysts play the most pivotal role in determining catalytic performance during the electrocatalytic CO_2RR. Until now, various nanomaterials — such as metals [7], metal oxides [8,9], single-atom catalysts [10–12], metal-organic frameworks [13–15], and two-dimensional (2D) layered compounds [16–18] — have been developed as potential nanocatalysts to drive the CO_2RR. Among these materials, metal nanocatalysts are particularly promising due to their high catalytic activity [19], excellent electrical conductivity [20], tunable electronic structure [21], and diverse catalytic products [22,23]. Over the past years, a number of metal nanocatalysts, such as Ag [24], Au [25], Pd [26], and Cu [27], with various nanostructures have been developed for the CO_2RR. To enhance electrocatalytic performance, previous reports mainly focused on the controlled synthesis of metal nanomaterials by tuning their compositions, dimensions, shapes, sizes, and architectures. Recently, phase engineering of nanomaterials (PEN) [28] has emerged as a promising strategy to regulate the properties of metal nanocatalysts towards the CO_2RR.

Although metal nanocatalysts generally crystalize in their thermodynamically stable phases, it has become feasible to acquire metal nanocatalysts with unconventional phases in particular experimental conditions [28]. By engineering the way atoms or ions are packed, metal nanocatalysts can present different phases and thus different catalytic properties [29]. Therefore, tuning the phases of metal nanocatalysts is becoming increasingly attractive for enriching the crystal structures of metals, regulating CO_2 catalytic pathways, and boosting catalytic performance.

In this review, we summarize the most recent developments in phase engineering of metal nanocatalysts for the electrocatalytic CO_2RR (Fig. 1). Various synthetic strategies for controlling the crystal phases of metal nanocatalysts are first introduced. Then up-to-date CO_2RR performance based on unique metal nanocatalysts is summarized, with an emphasis on their catalytic activity, selectivity, and stability. Finally, our insights into the challenges and opportunities for phase engineering of metal nanocatalysts towards the CO_2RR are proposed.

2. Crystal structures of metal nanocrystals

Based on the product types, metal nanocatalysts for the CO_2RR can be divided into three main categories [22]. Main group metal nanocatalysts, such as Sn, Pb, Sb, In, and Bi, often produce formate [39], while some post-transition metal nanocatalysts, including Au, Ag, Zn, and Pd, mostly convert CO_2 into CO [40]. Uniquely, Cu-based nanocatalysts can promote the formation of multi-carbon species such as C_2H_4, C_2H_5OH, and C_3H_7OH [41].

Conventionally, metal nanocatalysts exhibit crystal structures identical to their bulk ones. Among the metals with excellent CO_2RR catalytic activities, most adopt close-packed crystal structures, including face-centered cubic (fcc) (e.g., Au, Ag, Pd, Cu, Pb) and hexagonal close-packed (hcp) (e.g., Co and Zn) structures (Fig. 2). The close-packed plane in the fcc structure (also known as 3C), $\{111\}_{fcc}$, adopts the typical "ABC" stacking sequence along its close-packed direction, while the stacking sequence of the close-packed plane in the hcp structure (2H type), $\{0001\}_{hcp}$, follows a periodic pattern of "AB". In addition to the close-packed crystal structures, some metal nanocatalysts for the CO_2RR crystalize in non-close-packed structures, such as body-centered cubic (bcc) (e.g., Fe), body-centered tetragonal (bct) (e.g., In and Sn), or rhombohedral (rho) structures (e.g., Sb and Bi). Compared to close-packed crystal structures, non-close-packed ones show more diverse symmetries and lattice parameters, which might lead to different catalytic behaviors. Interestingly, among these metal nanocatalysts, most main group metal nanocatalysts (except Pb) that favor formate production crystalize in non-close-packed crystal structures, such as bct Sn [42] and rho Bi [43].

Importantly, unconventional crystal phases of metals that are less energetically favored in the bulk state become attainable at the

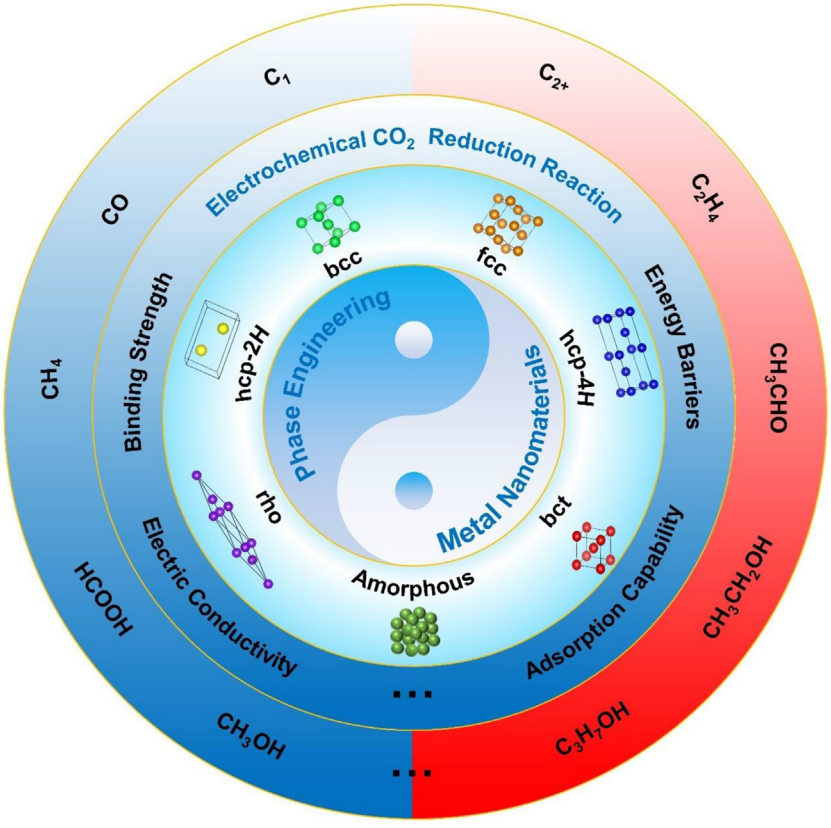

Fig. 2. Schematic overview of PEN for the electrochemical CO_2RR.

nanometer scale. For instance, the thermodynamically stable phase of Au in bulk size is fcc, while Au nanomaterials with unconventional 2H (2H type of hcp) [44], 4H (4H type of hcp) [45], and face-centered tetragonal (fct) [37] phases have been obtained. Besides the monometallic nanocatalysts, unconventional phases and phase transformation in bi- or multi-metallic nanomaterials could also be achieved [46]. In addition to well-crystalized structures, various crystallographic defects of metal nanocatalysts, such as amorphous structures without long-range periodic

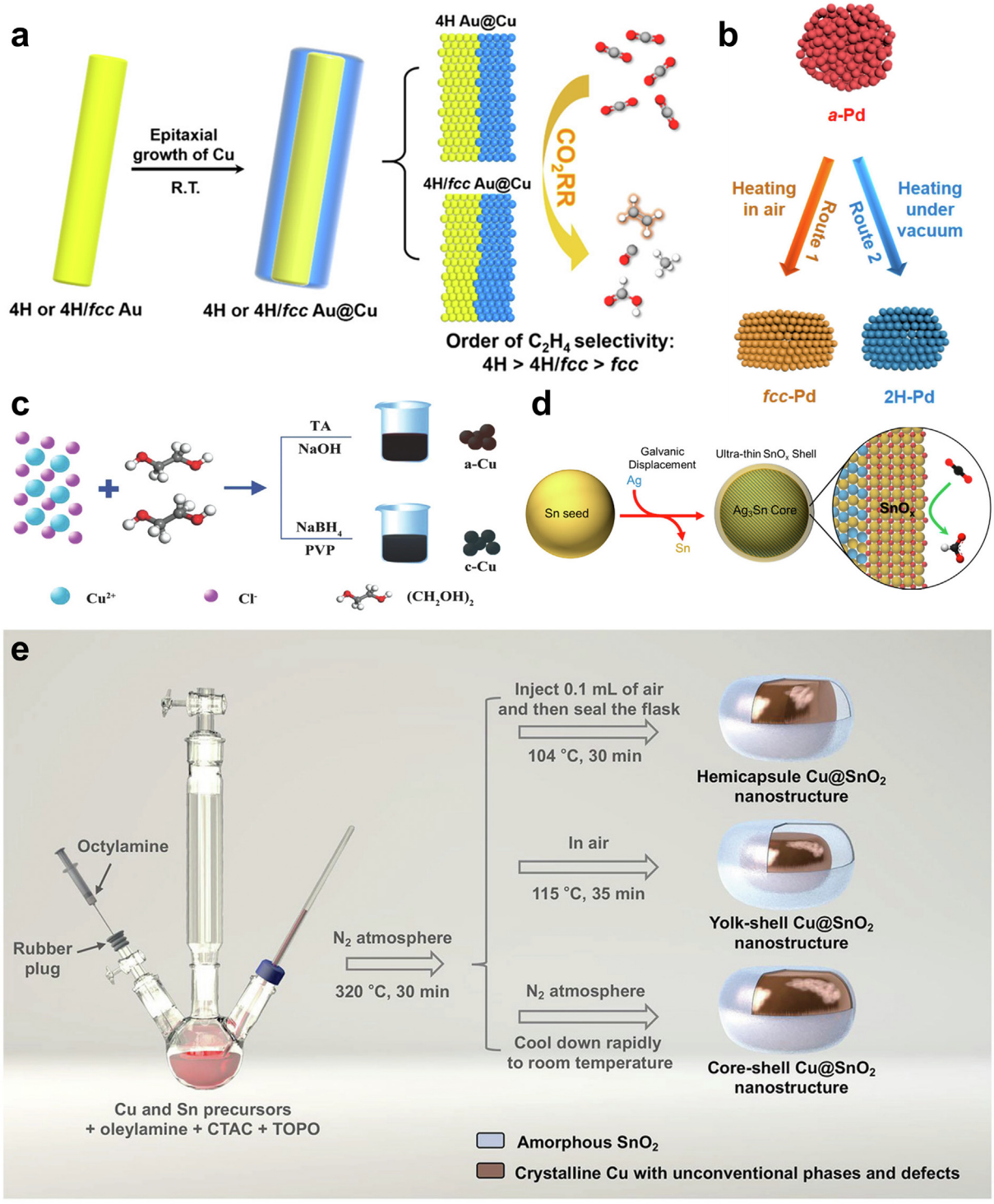

Fig. 3. (a) Schematic illustration of epitaxial growth of 4H and 4H/fcc Au@Cu core–shell nanocatalysts. Reproduced with permission from Ref. [36]. Copyright 2020, American Chemical Society. (b) Schematic illustration of phase transformation of amorphous Pd nanoparticles to fcc-Pd and 2H-Pd nanoparticles through different pathways. Reproduced with permission from Ref. [35]. Copyright 2020, American Chemical Society. (c) Schematic illustration of the preparation of amorphous Cu and crystalline Cu nanoparticles. Reproduced with permission from Ref. [32]. Copyright 2018 John Wiley & Sons, Inc. (d) Schematic illustration of the synthesis of bimetallic Ag–Sn core–shell nanocrystals with ultrathin, partially oxidized Sn shell. Reproduced with permission from Ref. [31]. Copyright 2017, American Chemical Society. (e) Schematic illustration of the synthesis of heterophase Cu nanostructures encapsulated by amorphous SnO_2 with different architectures. Reproduced with permission from Ref. [38]. Copyright 2022 John Wiley & Sons, Inc.

atomic arrangement [47], twin boundaries (TBs) [48,49], and stacking faults (SFs) [50], could also be employed to promote CO_2RR performance [51–53]. Moreover, recent research work has shown that the rational design and synthesis of metal nanocatalysts with more than one phase, i.e., heterophase, could be another efficient methodology to boost their activity and selectivity in the CO_2RR [34,35].

3. Synthetic strategies

To date, various wet-chemical synthesis strategies have been developed to enhance the catalytic performance of metal nanocatalysts in the CO_2RR. In this section, various PEN strategies, including the colloidal synthetic method, the electrochemical method, heat treatment, and some other approaches, are discussed, as well as some representative examples of controlling crystallographic defects such as TBs and SFs in metal nanocatalysts.

3.1. Colloidal synthesis

The colloidal synthesis method normally involves the chemical reduction of metal precursors in the presence of reducing agents, ligands/capping agents, and solvents in solution; advantages include fine control over the morphology, composition, size, and even simultaneous self-assembly of metal nanocatalysts [54,55]. Compared with other PEN strategies, colloidal synthesis is capable of yielding unconventional phases, TBs, and/or SFs in relatively high purity and large amounts under mild conditions [56,57]. Moreover, via the rational design of multi-step synthetic procedures, novel hetero-nanostructures with unconventional phases could be obtained [34].

The direct colloidal synthesis of metal nanocatalysts with unconventional crystal phases for the CO_2RR has been realized in Au [45], Pd [35], and Cu [36]. Taking Au as a representative example, 4H Au nanoribbons have been prepared using a colloidal synthesis method in a [Au(I)-oleylamine] complex system [58] in which 1,2-dichloropropane acted as an essential additive [45]. In the absence of 1,2-dichloropropane, only a mixture of twinned fcc Au nanoparticles and nanowires was obtained. Moreover, using the 4H Au nanoribbons as seeds, high-purity 4H Cu was also prepared via an epitaxial approach, which involved the rapid reduction of copper (II) nitrate by hydrazine hydrate in a suspension of 4H Au nanoribbons (Fig. 3a) [36]. Recently, our group has provided a phase transformation method to prepare 2H Pd nanoparticles from amorphous Pd nanoparticles [35]. During the synthesis, amorphous Pd nanoparticles were first synthesized by obtaining amorphous Pd nanoparticles from heating a mixture of palladium (II) acetate, oleylamine, toluene, and 1-dodecanethiol at 150 °C. Subsequently, an unconventional 2H phase could be transformed by heating the as-synthesized amorphous Pd nanoparticles in oleylamine under a high vacuum. In comparison, fcc Pd nanoparticles would be synthesized by heating the amorphous nanoparticles in air (Fig. 3b). In addition to unconventional phases of Au and Pd, amorphous Cu nanoparticles have also been prepared in solution by Duan et al. [32]. The preparation of amorphous Cu took place in ethylene glycol with the assistance of tannic acid as a weak reductant, while a strong reducing agent (sodium borohydride) led to the formation of crystalline Cu nanoparticles (Fig. 3c).

Besides unconventional crystal phases, metal nanocatalysts with abundant TBs and SFs have also been obtained using colloidal synthetic methods for the CO_2RR [58]. These crystallographic defects might lead to unusual adsorption behaviors on the catalyst surface and therefore affect the resultant CO_2RR pathways. For example, Hu et al. synthesized Ag nanocatalysts with well-defined dimensions and morphologies (nanowires and nanocubes) as model nanocatalysts and quantitatively analyzed their atom-specific catalytic activity on TBs [52]. The atom-specific activity of TB edges was catalytically greater than that of (100) surface atoms towards the overall CO_2RR. They adopted a polyol method from Silva et al. [59], in which penta-twinned Ag nanowires with continuous TBs along the longitudinal axis were synthesized by a bromide-mediated process. In another work, Choi et al. prepared oleylamine-capped five-fold twinned star decahedron Cu nanoparticles with multiple SFs and demonstrated their enhanced activity and selectivity for C_2H_4 production compared to commercial Cu nanoparticles [51]. The authors believed that high-density SFs were formed due to the release of internal stress during nanoparticle growth. In order to achieve the formation of TBs, a slow growth rate was maintained by using a weak reducing agent (L-ascorbic acid), a low concentration of Cu precursor, and a relatively low reaction temperature (130 °C).

Recently, heterophase nanocatalysts, in which more than one type of crystal phase coexists in a single nanostructure, have attracted abundant research interest. The presence of phase boundaries in heterophase nanostructures might lower the kinetic barriers in certain rate-limiting CO_2RR pathways and therefore promote catalytic activity and selectivity [34,36]. To date, various types of heterophases, including randomly distributed and well-defined heterophases, have been achieved by the colloidal synthesis method. For example, our group reported a high-yield colloidal synthesis of heterophase 4H/fcc Au nanorods with random alternating 4H and fcc crystal phases by heating gold (III) chloride hydrate dissolved in oleylamine at 70 °C for 17 h [60]. Using a similar method to prepare 4H Au@Cu core–shell nanoribbons, 4H/fcc heterophase Au@Cu nanorods were further synthesized by epitaxial growth of Cu on the 4H/fcc Au templates [36]. Since the Cu coating was uniform and thorough, the 4H and 4H/fcc Au@Cu core–shell nanomaterials could be used to investigate and provide insight into the phase-dependent CO_2RR behavior of Cu, while the Au cores did not directly participate in the catalytic reaction.

In addition to monometallic nanocatalysts, recently, bi- or multimetallic nanomaterials have also been prepared via the colloidal synthesis method. For example, bimetallic Ag–Sn [31] core–shell nanocrystals with ultrathin, a partially oxidized Sn (SnO_x) shell, were synthesized using a seed-mediated colloidal synthesis method. The authors used pre-synthesized Sn nanocrystals as seeds and controlled the subsequent galvanic replacement between Sn and Ag (I) (Fig. 3d). Interestingly, the dominant crystal phase in Ag–Sn was influenced by Sn content. At a low Sn concentration (10–20 at.%), the Ag–Sn binary alloy consisted of fcc Ag and disordered ξ-phase AgSn. As the Sn content increased to 24 at.%, an orthorhombic intermetallic ε-phase Ag_3Sn shell was obtained. As the Sn concentration further increased (to 60 at.%), the Ag–Sn alloy exhibited a heterophase containing both ε-phase Ag_3Sn and bct β-phase Sn. In another report, a unique crystalline/amorphous heterophase Bi–Sn nanostructure was prepared for generating formate through the CO_2RR [61]. The Bi–Sn nanoparticles with Bi-doped amorphous SnO_x shells were derived from $Sn_{0.80}Bi_{0.20}$ alloy nanoparticles, which were pre-synthesized via co-reducing Sn (II) and Bi (III) salts in a mixture of oleylamine and 1-octadecene in the presence of hexamethyldisilazane. Very recently, our group has prepared heterophase Cu nanostructures encapsulated by amorphous SnO_2 with different architectures via a colloidal synthesis method (Fig. 3e) [38]. Cu (II) acetylacetonate and Sn (II) chloride dihydrate were heated in a mixed solution containing oleylamine, hexadecyltrimethylammonium chloride, and trioctylphosphine oxide at 150 °C under a N_2 atmosphere. After the injection of octylamine, the mixture was heated to 320 °C. A series of Cu@SnO_2 hybrid structures, including hemicapsule, yolk–shell, and core–shell nanostructures, were obtained by controlling the temperature and atmosphere of the post-treatment process. Impressively, in all these nanostructures, Cu cores exhibited a unique heterophase structure composed of fcc, 2H, 4H, and 6H (6H type of hcp) phases, together with abundant TBs and STs.

3.2. Electrochemical synthesis

The electrochemical synthesis method presents unique advantages for designing and fabricating electrocatalysts, as it is not only capable of scalable synthesis and direct substrate-based fabrication of nanocatalysts [62], but also unique in yielding porous metal nanocatalysts and

high-index-facet metal nanocrystals [63–65]. For example, a series of high-index-facet noble metal nanocrystals has been synthesized via electrochemical methods based on square-wave potential [66,67]. As such, the electrochemical synthesis method is believed to demonstrate promising potential in realizing PEN, particularly in the direct synthesis of various electrocatalysts. It is possible to tailor the phases of metal nanocrystals by tuning various parameters during electrochemical syntheses, such as electrolyte composition, substrate surface, and applied potential.

Recently, in situ electrochemical structural tuning of nanocatalysts [68–70] during electrocatalysis has received intensive attention. Some essential properties of metal nanocatalysts, such as electronic structure

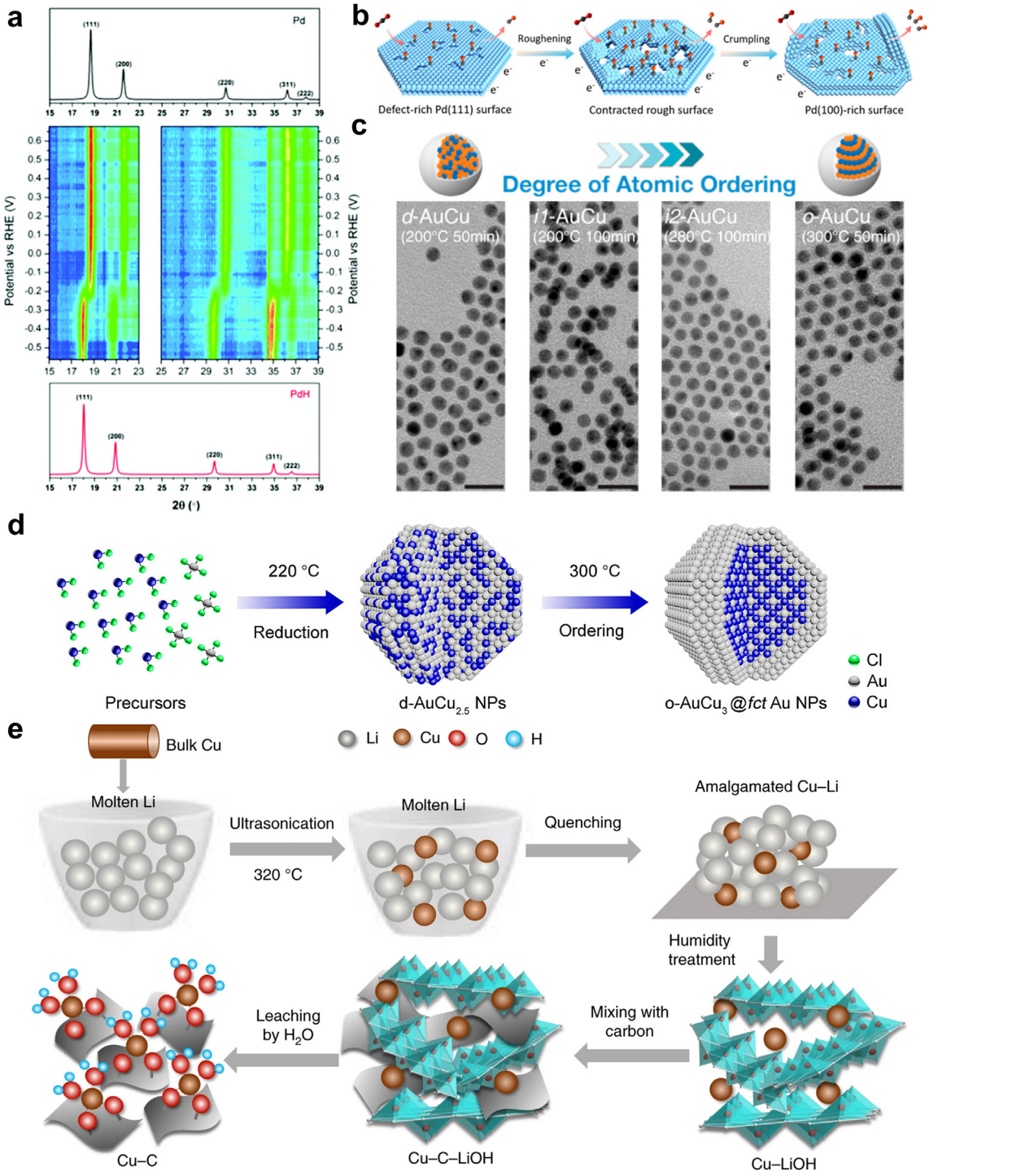

Fig. 4. (a) Contour profile of in situ XRD patterns of Pd nanocatalysts under linear sweep voltammetry from 0.68 to −0.56 V (*vs.* RHE) in CO_2-saturated 0.5 M $NaHCO_3$ solution. Reproduced with permission from Ref. [75]. Copyright 2017, Royal Society of Chemistry. (b) Schematic illustration of surface roughening and amorphization of ultrathin Pd nanosheets during long-term electrolysis. Reproduced with permission from Ref. [77]. Copyright 2020 John Wiley & Sons, Inc. (c) Transmission electron microscopy (TEM) images of Au–Cu bimetallic nanoparticles synthesized under various conditions with different degrees of atomic ordering. Scale bar, 20 nm. Reproduced with permission from Ref. [81]. Copyright 2017, American Chemical Society. (d) Schematic illustration of the synthesis of fct Au overlayers on intermetallic $AuCu_3$ nanocrystals. Reproduced with permission from Ref. [37]. Copyright 2021, American Chemical Society. (e) Schematic illustration of the preparation of carbon-supported Cu nanocatalysts by an amalgamated Cu–Li method. Reproduced with permission from Ref. [83]. Copyright 2020, Nature Publishing Group.

[71] and lattice strain [72], can be tailored by this strategy. For instance, by the in situ reduction of oxidized Cu during the CO_2RR, abundant grain boundaries were created in the Cu nanocatalysts, resulting in enhanced activity and selectivity for producing multi-carbon products [73,74]. In addition to designing and tailoring the crystallographic structures of metal nanocatalysts via electrochemical treatment, it is essential to note that some nanocatalysts undergo in situ phase transformation during electrochemical tests. Recently, Sheng et al. utilized in situ X-ray absorption spectroscopy and in situ X-ray diffraction to study the in situ phase transformation from fcc Pd to β-phase PdH during CO_2RR testing (Fig. 4a) [75]. Compared to the fcc Pd, the β-phase PdH showed much weaker adsorption strength with *CO, indicating enhanced anti-poisoning capacity towards CO. In another work, Gao et al. reported that the phase transformation behavior of Pd nanoparticles was influenced by the magnitude of applied potential during the CO_2RR [76]. At less negative potentials (above −0.2 V versus (*vs.*) reversible hydrogen electrode (RHE)), the formation of a layer of H-adsorbed Pd on the PdH_x cores with mixed α and β phases was identified, while at potentials more negative than −0.5 V (*vs.* RHE), the formation of a Pd layer on the β-phase PdH_x core was observed. Besides the phase transformation from Pd to PdH_x, partial surface roughening and amorphization of ultrathin Pd nanosheets were also observed during long-term electrolysis (Fig. 4b) [77].

Electrodeposition is another effective strategy to prepare metal nanocatalysts with amorphous phase, heterophase, or crystallographic defects. For example, Bi nanocatalysts with high amorphous phase content were prepared by Medina-Ramos et al. via electrodeposition on a glassy carbon disk electrode in a CO_2-saturated acetonitrile solution containing 300 mM imidazolium-based ionic liquid [78]. In another work, heterophase crystalline/amorphous Cu–In dendrites with an ~5 nm thick amorphous overlayer were electrodeposited on Au-sputtered Si substrate in 0.5 M H_2SO_4 containing Cu (II) and In (III) salts [79]. The dendritic morphology could be affected by the In content, giving tunable CO/H_2 selectivity to the Cu–In nanocatalysts in the CO_2RR. Besides amorphous and heterophase structures, programmed electrodeposition can also induce the formation of defect-rich nanocatalysts. For instance, Tang et al. applied a pulsed electrodeposition method to prepare Cu nanocatalysts with highly dense TBs with a twin width of 16 nm [80]. The TB density could be further controlled (the most probable twin width ranged from 16 to 265 nm) by annealing treatment at different temperatures.

3.3. Heat treatment

Heat treatment represents another important method that can tailor the atomic arrangement of metallic nanocatalysts. In particular, bimetallic nanocatalysts with controlled phases, including phase-separated alloys as well as ordered intermetallic and disordered alloys, have been obtained by thermal annealing of pre-synthesized nanocrystals. One representative work is a phase-dependent activity study of bimetallic Cu–Pd nanocatalysts with varied phase patterns [46]. Disordered Cu–Pd alloy nanoparticles were first synthesized by one-pot colloidal synthesis, and then annealed under a pure H_2 atmosphere at high temperature, facilitating the phase transformation to an ordered Cu–Pd intermetallic structure. The phase-separated Cu–Pd nanoparticles were synthesized by separating the reduction sequence of Pd and Cu precursors during the colloidal growth. These Cu–Pd nanocatalysts with adjustable compositions from $CuPd_3$ to Cu_3Pd were used to investigate the effects of phase and composition on their catalytic performances for the CO_2RR. Recently, Kim et al. discovered the disorder-to-order transformation of Au–Cu bimetallic nanoparticles via a thermal annealing process and investigated the effects of atomic ordering degree on the CO_2RR (Fig. 4c) [81]. Specifically, it was found that heat treatment would partially convert disordered Au–Cu nanoparticles into an ordered phase at 300 °C with ~80% of the atoms in the ordered lattice positions. Using a similar methodology, Jia et al. studied the phase transformation of Pd_3Bi from intermetallic to solid solution alloy upon thermal annealing at 500 °C for 2 h under N_2. It is worth noting that this solid solution phase was not expected in the Pd–Bi phase diagram. The authors presumed that the size effect of Pd_3Bi nanoparticles might be an important reason for the formation of this unconventional phase [82]. In another work, Yu et al. synthesized unconventional fct Au overlayers on intermetallic $AuCu_3$ nanocrystals [37]. The $AuCu_{2.5}$ nanocrystals were first prepared by the colloidal synthesis method and then annealed in oleylamine solution at 300 °C for 1 h to produce intermetallic $AuCu_3$ nanoparticles with 3–4 atomic overlayers of Au in the fct phase (Fig. 4d). The authors proposed that the formation of metastable fct Au may have derived from the interfacial strain between the Au overlayer and the intermetallic $AuCu_3$ core.

3.4. Other methods

Apart from the aforementioned methods, some other approaches have also been applied to achieve PEN of metal nanocatalysts for the CO_2RR. Using an alloying–dealloying methodology, unconventional phases of Cu-based nanocatalysts have been obtained. For example, Xu et al. prepared several carbon-supported Cu nanocatalysts with different Cu loadings by an amalgamated Cu–Li method [83]. The unique synthesis procedure involved dissolving bulk Cu in molten lithium, converting Li to LiOH under humidified air, blending with carbon, and finally leaching away LiOH with water (Fig. 4e). When the loading content of Cu was 0.4 wt.%, Cu atoms existed as isolated single atoms. As the Cu content increased to 0.8 wt.%, isolated Cu single atoms and Cu clusters were formed. With the Cu loading further increased to 1.6 wt.%, a mixture of highly dispersed Cu single atoms and amorphous Cu nanoclusters was observed. The authors found that the migration and aggregation of Cu were remarkably weakened by the carbon blending and LiOH leaching, so most of the Cu atoms were able to stay atomically dispersed. In another recent work, Hu et al. also used an alloying–dealloying method to synthesize amorphous CuTi alloys with coordinatively unsaturated Cu sites for the production of multi-carbon liquid feedstock via the CO_2RR [84]. The amorphous CuTi alloys with varied compositions were obtained by first mixing and melting Cu and Ti granules in controlled stoichiometric ratios and then rapidly quenching these in an argon atmosphere, followed by an etching process in a 5% HF solution to dissolve the superficial Ti atoms and obtain the final Cu-insufficient amorphous CuTi phase.

4. Brief discussion of reaction pathways of the CO_2RR

CO_2 usually exhibits a stable state due to its linear and centrosymmetric molecular structure [85]. To drive the CO_2RR efficiently, CO_2 molecules should be absorbed and activated on active sites to form proper chemical intermediates [86]. As the chemical conversions occur on the surface of catalysts, material structures, compositions, and surface properties play a key role in determining the CO_2 conversion efficiencies towards different products. Moreover, tuning catalyst structures and compositions as well as having a fundamental understanding of the surface reactions hold the key to realizing the full potential of many promising electrocatalysts.

Different types of metal catalysts show diverse adsorption strengths and configurations with different intermediates, thus generating diverse products in the CO_2RR (Fig. 5). The reaction pathways and mechanisms for generating C_1 and C_{2+} products during the CO_2RR on metal nanocatalysts have been well explored experimentally and theoretically [87]. After the initial CO_2 activation to $CO_2^{\cdot-}$ radical, *CO is normally regarded as the primary intermediate for major value-added chemicals [88], such as CO and alcohols, while *CHO is considered the in-process intermediate for CH_4 and CH_3OH [89]. Non-close-packed crystal structures might favor the formation pathway to formyloxyl (*OCHO) species [2,39]. By comparison, most metal nanocatalysts with close-packed crystal structures might facilitate the formation of carboxyl (*COOH)

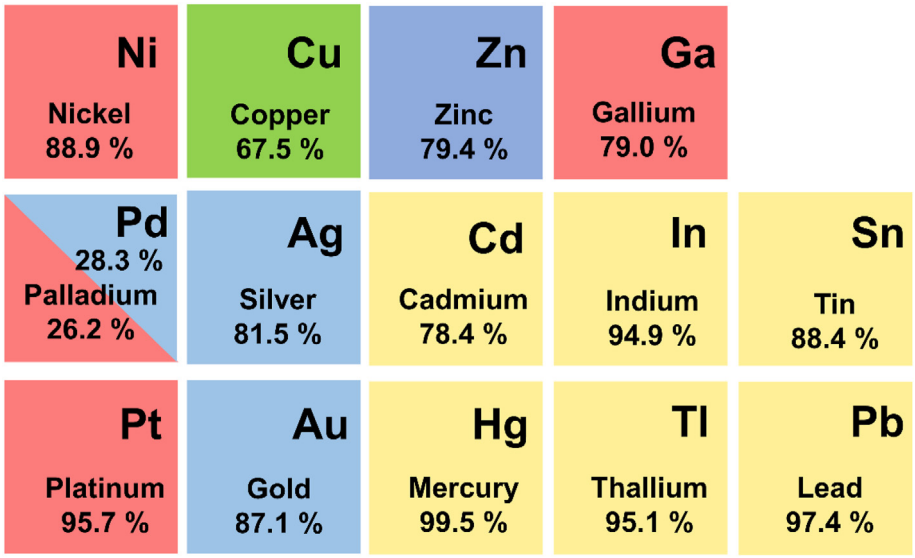

Fig. 5. Periodic table of metal catalysts for CO_2RR, and corresponding Faradaic efficiencies (FEs) of the major catalytic products [94,95]. The products are distinguished by different colors, i.e., H_2 (red), CO (blue), formate (yellow), hydrocarbon (green).

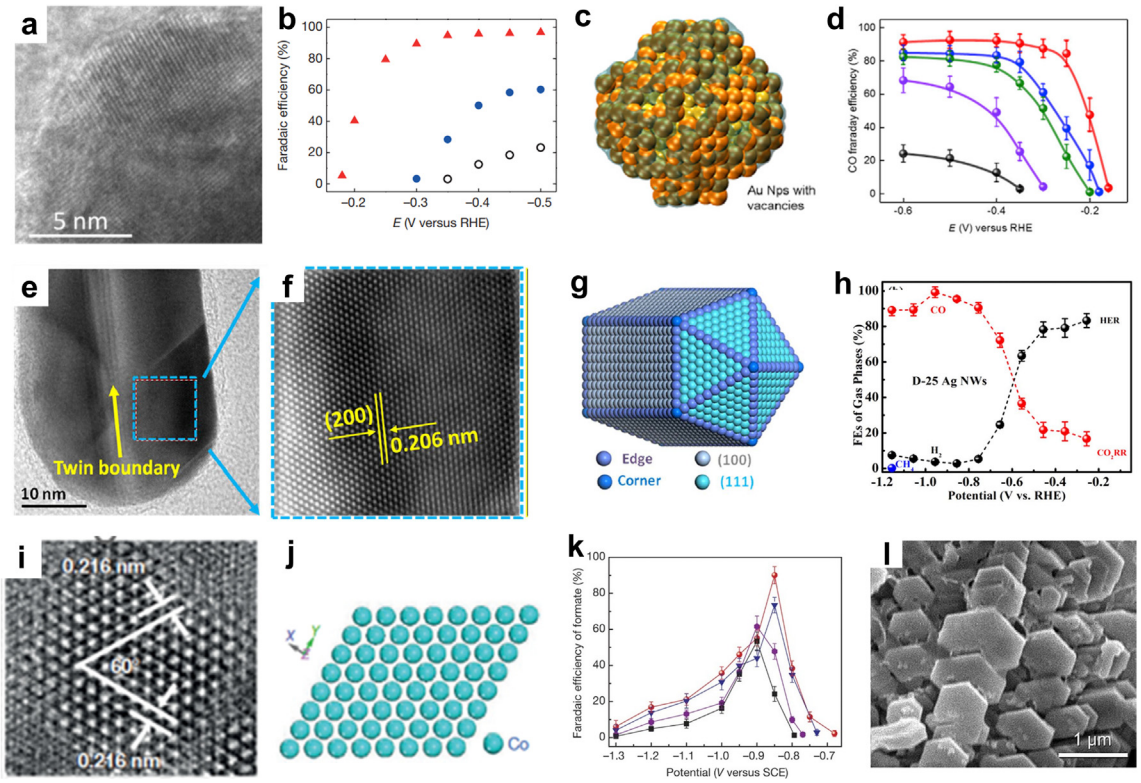

Fig. 6. (a) High-resolution Transmission Electron Microscope (HRTEM) image of Au needle tip, indicating no obvious facets or adatoms. (b) CO FEs on Au needles (red), rods (blue), and particles (black) at −0.1 to −0.5 V (*vs.* RHE). Reproduced with permission from Ref. [100]. Copyright 2016, Nature Publishing Group. (c) Schematic atomic models of Au nanoparticles with vacancies. (d) CO FEs on 3 nm (red), 4 nm (blue), and 5 nm (green) Au quantum dot-derived Au nanocrystals, Au nanoparticles (violet), and Au pentagonal nanoparticles (black) at different applied potentials ranging from −0.1 to −0.6 V. Reproduced with permission from Ref. [101]. Copyright 2019, Cell Press. (e, f) HRTEM images of Ag nanowires with a diameter of 25 nm. (g) Schematic drawing of 5-fold twinned Ag nanowires. (h) FEs of all gas-phase products over 5-fold twinned Ag nanowires with a diameter of 25 nm. Reproduced with permission from Ref. [102]. Copyright 2018, Elsevier. (i) Enlarged HRTEM images of hexagonal Co; (j) the related schematic atomic models, clearly showing a distinct atomic configuration corresponding to hexagonal Co. (k) FEs of formate at each given potential for partially oxidized Co with 4-atom-thick layers (red), Co with 4-atom-thick layers (blue), partially oxidized bulk Co (violet), and bulk Co (black). Reproduced with permission from Ref. [105]. Copyright 2016, Nature Publishing Group. (l) Surface morphology of prepared h-Zn nanocatalysts. Reproduced with permission from Ref. [107]. Copyright 2016 John Wiley & Sons, Inc.

intermediate, rendering the kinetically more favored CO_2-to-CO pathway [90]. Some post-transition metal nanocatalysts, such as Au, Ag, Pd, and their alloys, typically catalyze the electrochemical CO_2RR to CO [91], and main group metals such as Sn and In prefer to produce formate through the CO_2RR. Nanocrystalline Cu and Cu-based nanocatalysts are typically favorable for producing C_{2+} products such as hydrocarbons and oxocarbons through the CO_2RR. Promisingly, with the high selectivity and efficiency of CO_2-to-CO conversion, electrocatalytic upgrading of CO, instead of CO_2, to higher-value C_2 (ethylene) [92] or C_3 (propanol) [93] feedstocks has been well investigated as another attractive alternative to producing multi-carbon products.

Importantly, nanomaterials with unconventional phases can greatly enrich the catalyst library and bring extra opportunities to further improve CO_2RR performance. For instance, the atomic packing configuration of the unconventional phase is different from that of its conventional counterpart, which may show distinct binding strength towards CO_2 and intermediates. Therefore, investigations into metal nanocatalysts with unconventional phases for the CO_2RR may yield better mechanistic understandings on the structure–property relationship.

5. Phase engineering of metal nanocatalysts for the CO_2RR

As electrochemical reactions occur on the surface of nanocatalysts, catalytic CO_2RR performance is significantly affected by their surface structures, which can ultimately be affected by their crystal structures. To date, most reported metallic nanocatalysts adopt their thermodynamic stable phase, similar to their bulk counterparts [96]. However, recent studies on PEN have demonstrated the great potential of unconventional phases for enhancing the electrocatalytic performance of metal nanocatalysts [97]. In addition, as a unique type of phase, the amorphous structure with a highly disordered atomic arrangement has also attracted considerable interest in electrocatalysis.

5.1. Metal nanocatalysts with conventional phases for the CO_2RR

The conventional phase of metals typically represents their thermodynamically stable phase in bulk size. In this section, metal nanocatalysts with conventional phases, including representative transition metals and main group metals, are introduced. As a special class of transition metal nanocatalyst, Cu nanocatalysts are discussed separately. Some representative bimetallic structures are presented at the end of the section.

5.1.1. Transition metal nanocatalysts

Transition metal nanocatalysts have drawn extensive attention in electrocatalysis due to their outstanding stability, high activity, and electrical conductivity. A number of transition metals, including Au, Ag, Zn, and Pd, have been engaged to drive the CO_2RR [98].

fcc transition metal nanocatalysts: Au is one of the most efficient nanocatalysts for generating CO in the electrocatalytic CO_2RR [99]. To date, various Au nanostructures have been developed as highly efficient CO_2RR electrocatalysts [97]. For example, Liu et al. reported that fcc Au nanoneedles (Fig. 6a) prepared by an electrodeposition method displayed a Faradaic efficiency (FE) of about 95% towards CO at −0.35 V (*vs.* RHE) in CO_2-saturated 0.5 M $KHCO_3$ pH=7.2, which is much higher than that of Au nanorod and nanoparticle counterparts (Fig. 6b) [100]. Au needles also demonstrated stable current density at a potential of −0.35 V for 8 h. The superior performance was ascribed to the sharp tip of Au nanoneedles. Similar results were also demonstrated for fcc Pd nanoneedles. Compared with Pd nanoparticles, nanorods, and oxide-derived noble metal counterparts, the Pd nanoneedles exhibited a stable current density of 10 mA cm^{-2} at −0.2 V and a $FE_{formate}$ of 91% at −0.2 V (*vs.* RHE) throughout the electrocatalytic process [100]. Simultaneously, it was demonstrated that the Pd(100) crystallographic planes showed higher catalytic activity than the (111) planes because of its comparatively low binding strength towards CO [77]. These promising results motivated strong interest in tuning the structures and crystal faces of fcc noble metal nanocatalysts for electrocatalysis. Thus, the introduction of vacancies into noble metal nanocrystals (quantum dot-derived nanocatalysts) was developed to efficiently tune the structures of fcc noble metals for the CO_2RR. Liu et al. reported the synthesis of quantum dot-derived Au nanocrystals (Fig. 6c), which possessed a high density of homogeneously dispersed atomic defects and vacancies [101]. Compared with other control samples (4 nm Au nanocrystals, 5 nm Au nanocrystals, Au nanoparticles, and Au pentagonal nanoparticles), the 3 nm quantum dot-derived Au nanocrystals exhibited the highest FE (~95%) for producing CO (Fig. 6d). It is noteworthy that the onset of the CO_2RR occurred at a potential of −0.16 V (*vs.* RHE) on the 3 nm quantum dot-derived Au nanocrystals, which was significantly lower than that of their nanoparticle counterpart [101]. Similar results were also demonstrated for dot-derived Pd nanocrystals. Apart from Au and Pd, other fcc transition metals with similar structures, such as Ag [24], have also shown high performance towards the CO_2RR. Various crystallographic defects of metal nanocatalysts, such as TBs [34,35] and SFs [85], could also be employed to promote their CO_2RR performance. For instance, 5-fold twinned Ag nanowires with rich TBs (Figs. 6e–g) possessed remarkably enhanced FEs for producing CO over a broad potential range (−0.756 to −1.156 V) with a maximum FE value of 99.3% at −0.956 V (*vs.* RHE) (Fig. 6h) [102].

Despite the importance of noble metal nanocatalysts, most of them produce H_2 gas at low reduction potentials, lowering the FE of the CO_2RR. Moreover, the high cost and low utilization of noble metals have greatly limited their practical application. Therefore, non-noble metal nanocatalysts that are cheap and possess comparably high activity are receiving increasing attention.

hcp transition metal nanocatalysts: Co (with conventional hcp phase) is a promising electrocatalyst because it has loosely bonded d-electrons and high electrical conductivity [103]. Recently, Yin et al. reported that ferromagnetic hcp Co nanosheets were selective to ethanal (CH_3CHO) in the CO_2RR [104]. The Co nanosheets exhibited a high FE for CH_3CHO of ~60% at −0.4 V (*vs.* RHE) (the total FE for CH_3CHO, C_2H_5OH, and CH_3OH was 82%). Moreover, Gao et al. synthesized four-atomic-layer thick Co nanosheets with an hcp phase and an oriented (001) surface (Figs. 6i and j) through a ligand-confined growth strategy [105]. It was discovered that partially oxidized Co nanosheets could drive the CO_2RR with a maximum FE of 90.1% towards formate at −0.85 V *vs.* saturated calomel electrode (SCE) in 0.1 M Na_2SO_4 (pH ≈ 6) (Fig. 6k). Notably, the catalytic performance of the partially oxidized Co nanosheets was superior to that of pure Co nanosheets, bulk Co with partial oxidation, and bulk Co under the same reaction conditions. Similarly, Zn-based nanomaterial, with hcp phase as the conventional phase, is another economical alternative for the CO_2RR. For example, Jeon et al. synthesized Zn nanoparticles with sizes ranging from 1.7 to 6.8 nm via an inverse micelle encapsulation method [106]. The experimental results showed that the main products were CO and H_2 for all these samples, with about 5% formate as a minor product. The as-prepared Zn nanoparticles with sizes from 3 to 5 nm showed a high FE_{CO} of ~70% at −1.1 V (*vs.* RHE) in 0.1 M $KHCO_3$. In another report, hierarchical hcp Zn nanocatalysts were prepared by an electrodeposition method and demonstrated a high FE of 85.4% at −0.95 V (*vs.* RHE) for CO production, delivering 60 times the CO partial current density of Zn foil (Fig. 6l) [107]. It was found that the Zn(101) facet contributes to CO formation at lower potentials by effectively stabilizing a *COOH intermediate, whereas the Zn(002) facet is conducive to H_2 evolution.

5.1.2. Cu nanocatalysts

fcc Cu nanocatalysts: Cu is one of the most attractive monometallic electrocatalysts for its unique ability to convert CO_2 to multi-carbon and hydrocarbon products [108,109]. The conventional phase of Cu is fcc, which has been widely investigated for the CO_2RR [110].

To date, engineering the surface features of Cu, such as facets, grain boundaries, etc., has been the focus to optimize the CO_2RR performance of fcc Cu nanocatalysts [111]. For instance, Luc et al. introduced the

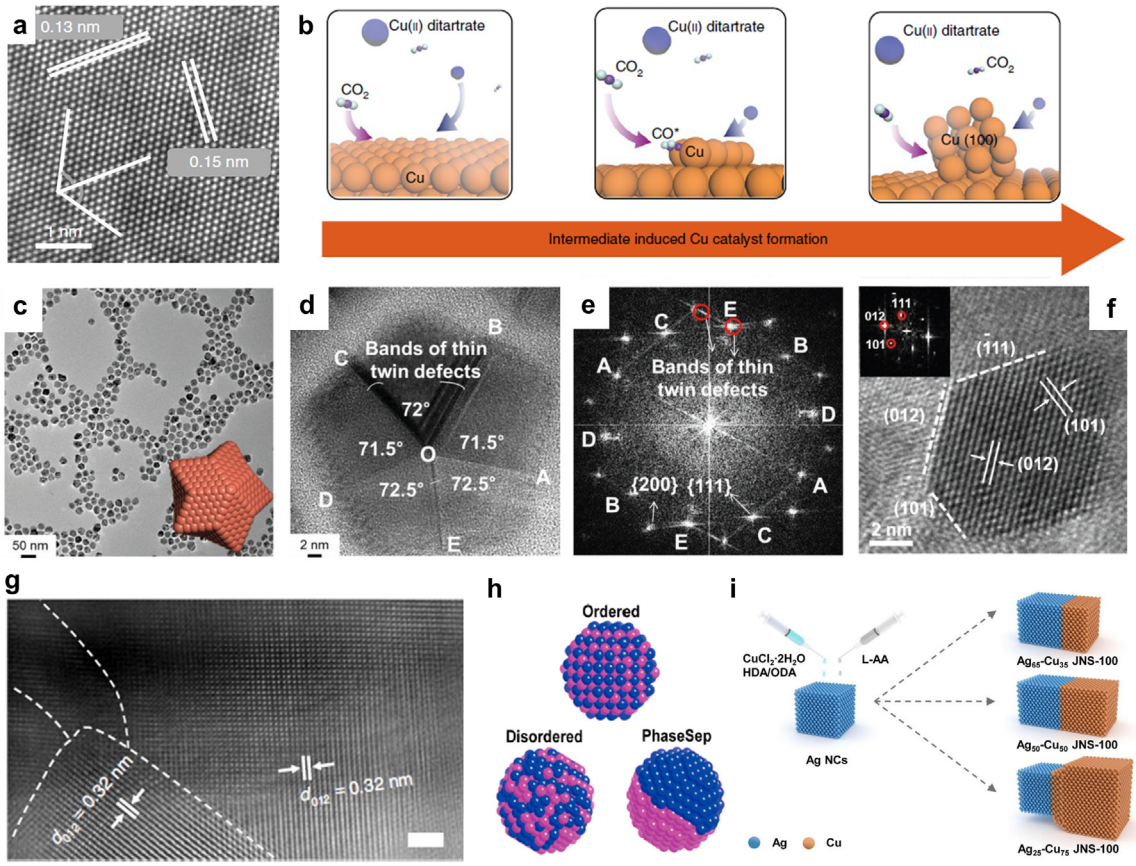

Fig. 7. (a) The HRTEM image shows the basal plane projection of a Cu nanosheet. Reproduced with permission from Ref. [112]. Copyright 2019, Nature Publishing Group. (b) A schematic illustration of intermediate (for example, CO*) adsorption leading to a high proportion of Cu(100) facets in the formed catalyst. Reproduced with permission from Ref. [122]. Copyright 2020, Nature Publishing Group. (c) Low-magnification TEM image of star decahedron Cu nanoparticles (inset is a schematic of the atomic structure). (d) HRTEM image of a 5-fold twinned star decahedron Cu nanoparticles. (e) Five-fold twin symmetry in fast Fourier transform (FFT) images of star decahedron Cu nanoparticles. Reproduced with permission from Ref. [51]. Copyright 2018 John Wiley & Sons, Inc. (f) TEM image and its corresponding FFT of reduced mesoporous Bi nanosheets. Reproduced with permission from Ref. [43]. Copyright 2018 John Wiley & Sons, Inc. (g) HRTEM image of n-butyl lithium-treated Bi nanocatalysts. Grain orientations were observed in n-butyl lithium-treated Bi; scale bars=2 nm. Reproduced with permission from Ref. [116]. Copyright 2020, Nature Publishing Group. (h) Schematic of prepared CuPd nanoalloys with different structures. Reproduced with permission from Ref. [46]. Copyright 2017, Royal Society of Chemistry. (i) Schematic of synthesis and structural characterization of Ag–Cu Janus (JNS) nanostructures. HAD: 1-hexadecylamine; ODA: octadecylamine; L-AA: L-ascorbic acid; NCs: nanocubes. Reproduced with permission from Ref. [122]. Copyright 2022 John Wiley & Sons, Inc.

preparation of (111)-enclosed Cu nanosheets (Fig. 7a), which demonstrated a maximum FE of ~70% for C_{2+} products with a maximum acetate FE of ~48% in 2 M KOH [112]. In another work, Wang et al. prepared fcc Cu nanocubes by in situ electrodeposition of Cu under CO_2 flow, which preferentially exposed Cu(100) facets. The as-prepared sample showed 70% coverage by Cu(100) facets (Fig. 7b) and consequently achieved a FE of 90% for C_{2+} products at −0.67 V (*vs.* RHE), with a C_2H_4 FE of ~70% in 7 M KOH [113]. Chen et al. further found that the Cu(110) facet could promote the anhydrous dehydrogenation of CH_3OH, C_2H_5OH, and 1-propanol to their corresponding aldehyde products [114].

What is more, the introduction of rich TBs on the surface of Cu nanocrystals can also tune their surface activity and thus improve the CO_2RR performance. For example, star decahedron Cu nanoparticles with highly dense TBs prepared by Tang et al. showed high selectivity towards CH_4, with a FE of 59% at −1.6 V in 0.2 M $NaHCO_3$ electrolyte [80]. In another example, unique 5-fold twinned star decahedron Cu nanoparticles (Figs. 7c–e) with continuous TBs and multiple hcp SFs delivered a high $FE_{C_2H_4}$ of 50.7% at −0.98 V (*vs.* RHE) in 0.1 M $NaHCO_3$ electrolyte [51].

5.1.3. Main group metal nanocatalysts

rho and bct metal nanocatalysts: Bi typically crystalizes in the rho phase, and Sn typically shows the bct phase, both of which are attractive in electrocatalysis due to their low cost and non-close-packed structures [115]. Various nanostructures have been prepared, including clusters and nanosheets. For instance, Fan et al. prepared n-butyl lithium-treated Bi nanocatalysts with rich grain boundaries (GBs) (Fig. 7g) by using a chemical Li tuning method [116]. The GB-rich Bi nanocatalysts exhibited high activity, selectivity (maximum FE of ~97% at −0.77 V (*vs.* RHE)), and stability (~100 h) towards formate production. The abundant GBs and high surface area were mainly responsible for the enhanced catalytic performance. In another example, Yang et al. prepared 2D mesoporous Bi nanosheets that exhibited excellent $FE_{formate}$ of ~99% at −0.9 V (*vs.* RHE) and satisfactory stability (Fig. 7f) [43]. Based on the density functional theory (DFT) results, the (101) and (111) facets of Bi can stabilize the OCHO* intermediate, contributing primarily to formate production. Similarly, Sn nanosheets have been prepared and demonstrated an outstanding $FE_{formate}$ of 89% at −1.8 V *vs.* SCE [117].

5.1.4. Bimetallic nanocatalysts

Alloying or constructing bimetallic heterostructures can be effective methods to decrease the energy barriers of catalytic reactions and promote charge transfer during the CO_2RR, and eventually modulate the reaction pathways to achieve better performance towards target products. Specifically, these bimetallic electrocatalysts show significant advantages: (1) unique electronic structures that can regulate the binding

energy of major intermediates (e.g., *OCHO and *COOH) for the CO_2RR; (2) the capacity to integrate several electrochemical transformations in a single process to realize multi-step CO_2RR reactions; and (3) improved catalytic stability.

Cu has attracted considerable interest for building Cu-based bimetallic nanomaterials to tune the reaction pathways of the CO_2RR [89]. To date, a broad range of metals (e.g., Ag, Au, Co, Zn, Bi, etc.) have been successfully alloyed with Cu for the CO_2RR [118,119]. The choice of secondary metal is critical in tuning the adsorption energies of reaction intermediates and thus greatly affects the final catalytic performance. For example, it has been found that the integration of Bi with Cu can adjust the bonding strength of critical intermediates during the CO_2RR and give superior CO_2RR properties [120]. Zhang et al. reported the growth of lattice-dislocated Bi nanowires on a Cu foam by using in situ electrochemical transformation under thermal treatment in air. The nanocatalysts were active for CO_2 reduction towards formate formation with a low potential, attaining an $FE_{formate}$ of 95% at −0.7 V (*vs.* RHE) [121]. The high catalytic activity of the Cu–Bi electrode could be ascribed to the unique porous structure as well as the presence of lattice dislocations in the nanowires.

Importantly, by controlling the degree of atomic ordering and distribution of different metal elements in the bimetallic nanostructures, the catalytic performance can also be tuned. For example, Ma et al. designed bimetallic Cu–Pd nanocatalysts with different degrees of atomic ordering (ordered, disordered, and phase-separated) to compare their catalytic performance in 1 M KOH [46]. The ordered CuPd nanocatalyst exhibited superior FE for C_1 products (> 80%) (Fig. 7h). In contrast, the phase-separated CuPd and the disordered Cu_3Pd nanocatalysts showed better selectivity (> 60%) for C_2 chemicals than $CuPd_3$ and ordered CuPd nanocatalysts, demonstrating that the dimerization of C_1 intermediates may be more favored on surfaces with neighboring Cu atoms. Ma et al. recently investigated crystal phase-dependent CO_2RR performance towards C_2H_4 production by using Ag–Cu Janus nanostructures. Ag–Cu heterostructures with (100) crystallographic planes demonstrated high selectivity in the electrochemical CO_2RR towards C_{2+} products (Fig. 7i). The obtained Ag_{65}–Cu_{35} nanostructures

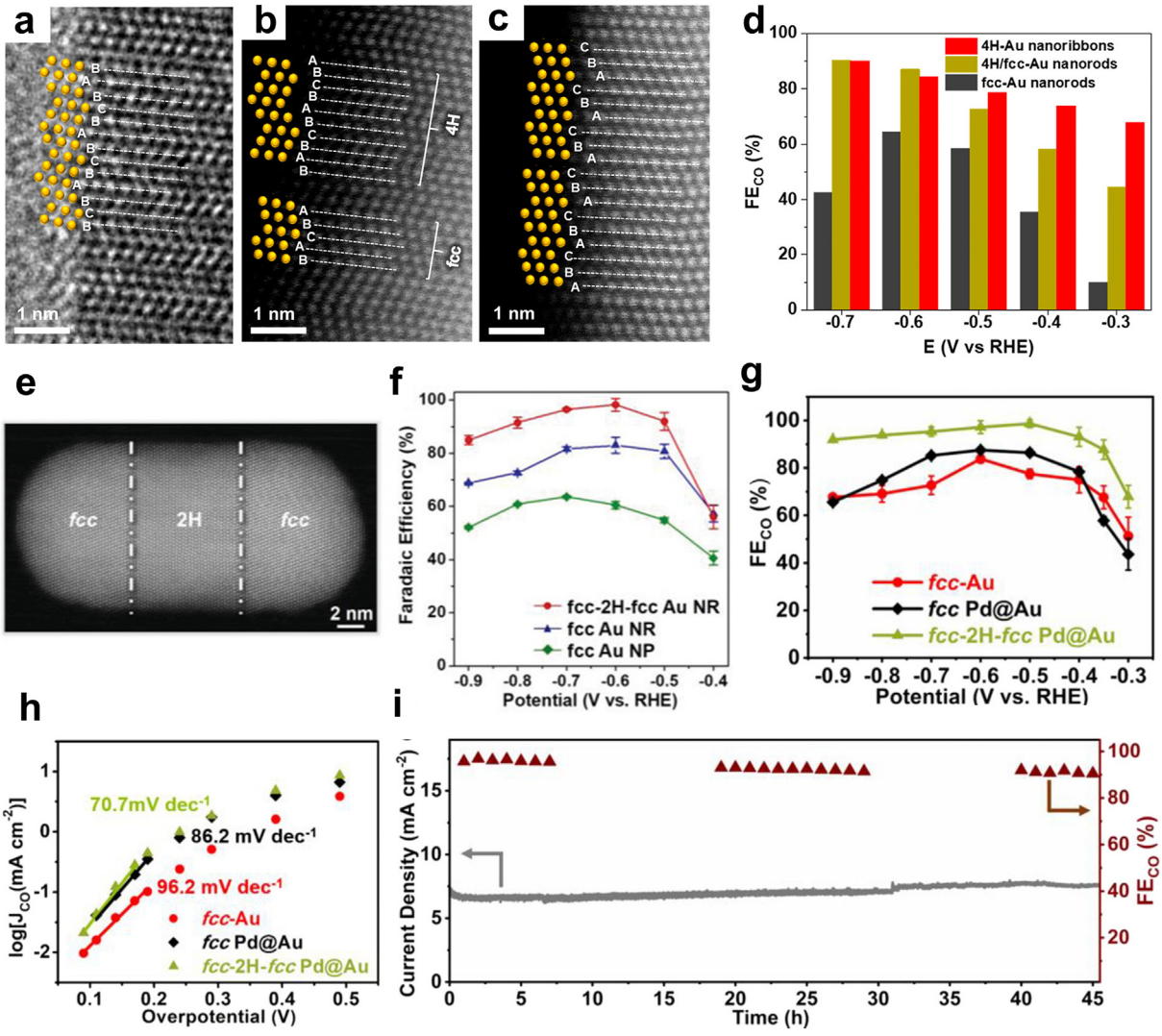

Fig. 8. HRTEM images of (a) 4H-Au nanoribbons, (b) 4H/fcc-Au nanorods, and (c) fcc-Au nanorods. (d) FE_{CO} of three types of Au nanocrystals for the CO_2RR. Reproduced with permission from Ref. [33]. Copyright 2020, American Chemical Society. (e) High-angle annular dark-field scanning TEM (HAADF-STEM) image of a heterophase fcc-2H-fcc Au nanorod. (f) The FE_{CO} of different Au nanostructures at potentials from −0.9 to −0.4 V (*vs.* RHE). Reproduced with permission from Ref. [34]. Copyright 2020, Nature Publishing Group. (g) FE_{CO} and (h) Tafel plots for the CO_2RR of fcc-2H-fcc Pd@Au nanorods, fcc Pd@Au nanoparticles, and fcc-Au nanorods. (i) Long-term stability testing of fcc-2H-fcc Pd@Au nanorods at −0.6 V (*vs.* RHE). Reproduced with permission from Ref. [35]. Copyright 2020, American Chemical Society.

exhibited a superior overall $FE_{C_2H_4}$ of 54% and a C_{2+} product FE of 72% in 0.1 M $NaHCO_3$ [122]. It was suggested that the binding energy between CO and Cu is higher than that of Ag. Thus, the CO intermediates formed on Cu accumulate in large quantities at the Ag–Cu interface, which favors C–C bond formation by coupling.

5.2. Metal nanocatalysts with unconventional crystal phases for the CO_2RR

With the recent development of PEN, a broad range of metal nanocatalysts with unique unconventional crystal phases have been prepared, demonstrating outstanding performance in the electrocatalytic CO_2RR.

5.2.1. Au nanocatalysts with unconventional crystal phases

To date, a variety of Au nanocatalysts with unconventional phases have been studied for the CO_2RR, including 4H [33], 4H/fcc heterophase [33], and well-defined fcc-2H-fcc heterophase [34]. By using 4H/fcc Au nanorods as a template, 4H/fcc Au@Pd nanorods were successfully prepared in high yield through a one-pot, facile, wet-chemical strategy [60]. The catalytic performance differences between the conventional fcc Au, the unconventional 4H Au, and the heterophase 4H/fcc Au were studied by Wang et al. (Figs. 8a–c), who found that the abundant undercoordinated sites were active towards the CO_2RR [33]. Interestingly, the unconventional 4H/fcc Au showed a FE_{CO} of 90% at −0.7 V (*vs.* RHE), which was much higher than the FE_{CO} of 64% at −0.6 V of conventional fcc Au nanorods (Fig. 8d). 4H Au nanoribbons also exhibited an excellent FE_{CO} of 90% at −0.7 V [33]. The catalytic performance differences between conventional fcc Au nanorods, unconventional 4H Au nanoribbons, and heterophase 4H/fcc Au nanorods indicated that the abundant undercoordinated sites were active towards the CO_2RR. A later study by Wang et al. [123] suggested that with proper surface modification, the CO_2RR performance of 4H/fcc Au nanorods could also be tuned. They prepared 4H/fcc Au nanorods modified with 5-mercapto-1-methyltetrazole (MMT) and demonstrated that the MMT activated the nanocatalyst surfaces of both fcc and 4H phases and lowered the reaction barriers. Very recently, a new type of heterophase Au — well-defined fcc-2H-fcc heterophase Au (Fig. 8e) [34] — was also studied for the CO_2RR. The fcc-2H-fcc Au nanorods showed a FE_{CO} of 98.2% at −0.6 V (*vs.* RHE) in 0.5 M $KHCO_3$, which was superior to their fcc counterparts towards CO production (Fig. 8f). Further, the partial current density (J_{CO}) for CO on the fcc-2H-fcc Au nanorods was significantly enhanced compared with fcc nanorods and nanoparticles. DFT calculations

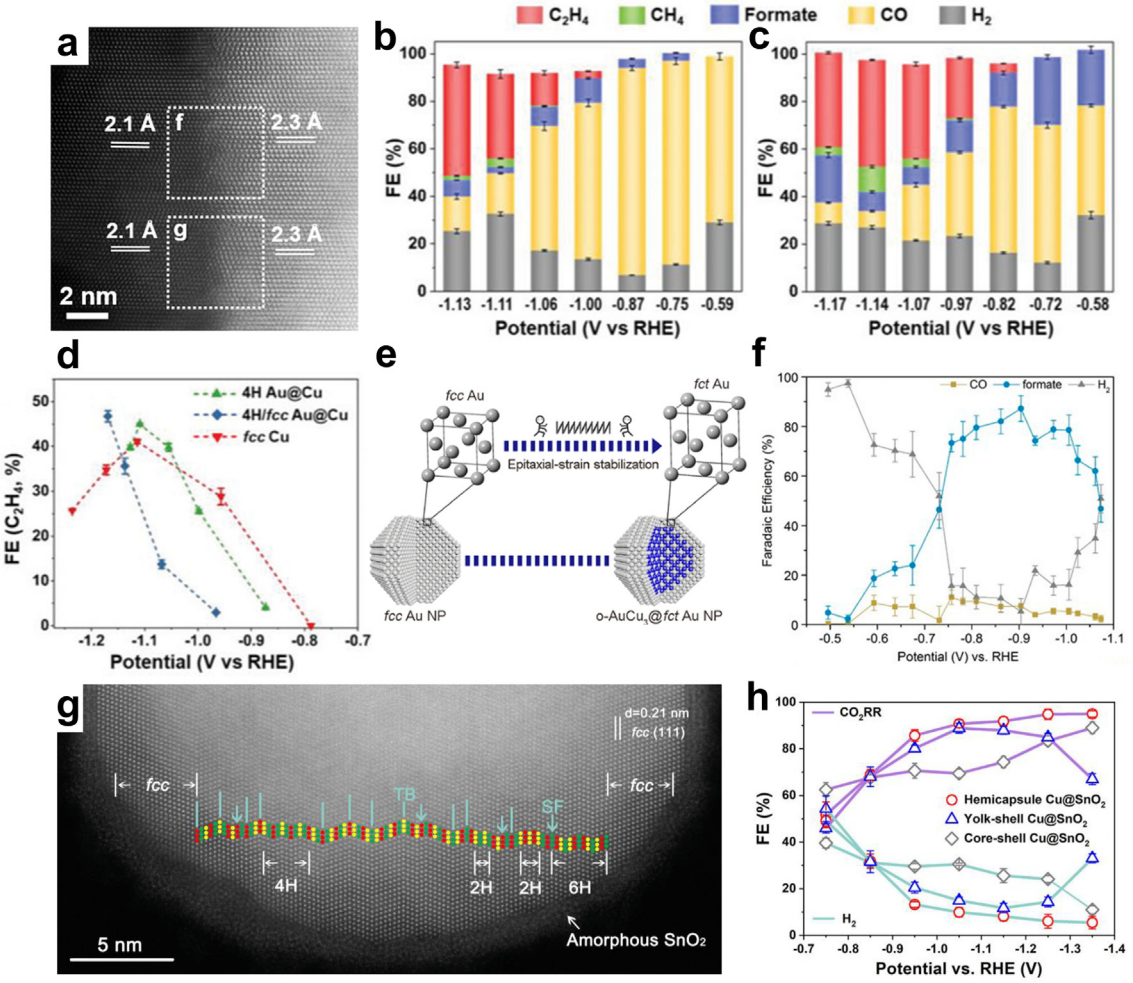

Fig. 9. (a) C_s-corrected scanning TEM (C_s-corrected STEM) image at the core–shell interface of 4H/fcc Au@Cu (b, c) FEs for various CO_2RR products obtained on 4H Au@Cu (b) and 4H/fcc Au@Cu (c) nanocatalysts. (d) FEs of C_2H_4 on 4H Au@Cu, 4H/fcc Au@Cu, and fcc Cu catalysts. Reproduced with permission from Ref. [36]. Copyright 2020, American Chemical Society. (e) Schematic illustration of the preparation of $AuCu_3$@fct Au core–shell nanoparticles and fcc Au nanoparticles. Reproduced with permission from Ref. [37]. Copyright 2021, American Chemical Society. (f) FE_{CO}, $FE_{formate}$, and FE_{H_2} of $Ag_{76}Sn_{24}$ nanocatalysts for the CO_2RR. Reproduced with permission from Ref. [31]. Copyright 2017, American Chemical Society. (g) Magnified aberration-corrected HAADF-STEM image of a representative hemicapsule Cu@SnO_2 nanostructure. The light cyan line and arrow represent TB and SF, respectively. (h) FEs of the CO_2RR and H_2 of the hemicapsule Cu@SnO_2, yolk–shell Cu@SnO_2, and core–shell Cu@SnO_2 nanostructures. Reproduced with permission from Ref. [38]. Copyright 2022, John Wiley & Sons, Inc.

illustrated that the free energies on 2H(110) and 2H(110)/fcc(101) surfaces are usually lower than on the corresponding fcc surfaces. It was further suggested that the reaction path on the fcc-2H-fcc Au surface included a single-electron transfer process and a subsequent rate-determining *COOH formation step.

Our group reported the synthesis of well-defined heterophase fcc-2H-fcc Pd@Au core–shell nanorods via a seeded growth method [35]. The FE_{CO} of the fcc-Au nanorods and fcc Pd@Au nanoparticles showed typical volcano-type plots with FE peaks located at −0.6 V, whereas the peak of the fcc-2H-fcc Pd@Au nanorods was located at −0.5 V (*vs.* RHE) (Fig. 8g). Note that the FE_{CO} of the fcc-2H-fcc Pd@Au nanorods remained at over 90% in a broad applied potential range between −0.4 V and −0.9 V. In addition, the highest FE_{CO} of the fcc-2H-fcc Pd@Au nanorods was ~98.7% at −0.5 V (*vs.* RHE) in 0.5 M $KHCO_3$, much higher than those of fcc-Au nanorods, fcc Pd@Au nanoparticles, and 2H-Pd nanoparticles. Moreover, the fcc-2H-fcc Pd@Au nanorods exhibited large J_{CO} from −0.4 to −0.9 V (*vs.* RHE). By normalizing the J_{CO} to the active surface areas, the fcc-2H-fcc Pd@Au nanorods illustrated a remarkably higher specific J_{CO} than the fcc Pd@Au nanoparticles and fcc-Au nanorods. The results indicated the superior intrinsic activity of the heterophase nanostructures. The Tafel slope of the fcc-2H-fcc Pd@Au nanorods was 70.7 mV dec^{-1} (Fig. 8h). In addition, the fcc-2H-fcc Pd@Au nanorods demonstrated excellent long-term durability during the electrochemical CO_2RR process. As shown in Fig. 8i, both the J_{CO} and the FE_{CO} decreased only slightly after 45 h of stability testing. It was therefore suggested that the unconventional 2H-Au and 2H/fcc phase boundaries in the fcc-2H-fcc Pd@Au nanorods were conducive to boosting the CO_2RR properties.

5.2.2. Cu nanocatalysts with unconventional crystal phases

In addition to Au, Cu nanocatalysts with unconventional phases have also been prepared and studied for the CO_2RR. By using 4H and 4H/fcc Au as templates, 4H Au@Cu and heterophase 4H/fcc Au@Cu nanocatalysts (Fig. 9a) were prepared, respectively [36]. Both samples were stable during the CO_2RR from −0.4 to −1.20 V (*vs.* RHE) in 0.1 M $KHCO_3$. Notably, 4H Au@Cu and 4H/fcc Au@Cu nanocatalysts with unconventional crystal phases exhibited outstanding overall CO_2RR FEs of ~88% at −0.75 V (*vs.* RHE) and ~91% at −0.82 V (*vs.* RHE), respectively (Figs. 9b and c). Both 4H and 4H/fcc Au@Cu nanocatalysts possessed outstanding CO_2RR current densities and low onset potentials, in contrast with their fcc Cu counterparts. Notably, the C_2 products, e.g., ethylene (C_2H_4), were obtained when more negative reduction voltages were applied. The excellent $FE_{C_2H_4}$ of 4H and 4H/fcc Au@Cu nanocatalysts reached 44.9% at −1.11 V (*vs.* RHE) and 46.7% at −1.17 V (*vs.* RHE), respectively (Fig. 9d). In addition, much higher C_2H_4 partial current densities were obtained when using the 4H and 4H/fcc Au@Cu nanostructures as CO_2RR catalysts rather than fcc Cu nanoparticles. DFT results illustrated that C_2H_4 generation was more favored on the surface of 4H phase and 4H/fcc interfaces, resulting in higher selectivity for C_2H_4. Therefore, it would be promising to continue developing unconventional structures of 4H and 4H/fcc Au@Cu to enhance their catalytic activity and C_2H_4 selectivity during the CO_2RR.

5.2.3. Other metal nanocatalysts with unconventional crystal phases

Up to now, several kinds of bimetallic nanocatalysts with unconventional phases, such as fct AuCu@Au [37] and core–shell Cu@SnO_2 [38], have been prepared and utilized for the electrocatalytic CO_2RR [124]. For example, Yu et al. reported the growth of $AuCu_3$@Au core–shell structures by growing metastable fct Au overlayers on intermetallic $AuCu_3$ nanocrystals (Fig. 9e) [37]. The fct Au overlayer (three to four atomic layers) was epitaxially coated on the surface of $AuCu_3$ due to interfacial strain between the Au layers and the intermetallic $AuCu_3$ core. The FEs for CO formation over $AuCu_3$@fct Au core–shell nanoparticles and fcc Au nanoparticles were determined at potentials between −0.6 and −1.0 V (*vs.* RHE). The atomically ordered $AuCu_3$@fct Au core–shell nanoparticles displayed superior selectivity in a wide potential window, in contrast with fcc Au nanoparticles, showing a higher CO FE of 94.5% at −0.8 V (*vs.* RHE) than that of fcc Au nanoparticles. What is more, Luc et al. demonstrated that the orthorhombic intermetallic ε-phase $Ag_{76}Sn_{24}$ nanocatalyst (Fig. 9f) could achieve remarkable electrochemical performance in the CO_2RR, with a maximum formate FE of 87.2% at −9.0 V (*vs.* RHE) [31].

Construction of metal-based heterostructures is another effective method to prepare metal nanocatalysts with unconventional phases and/or defects. Our group reported the synthesis of multi-phase crystalline Cu with unconventional crystal phases (e.g., 2H, 4H, and 6H) and defects (e.g., TBs and SFs) by a wet-chemical method. The multi-phased crystalline Cu was encapsulated by amorphous SnO_2 to form hemicapsule nanostructures (Fig. 9g) [38]. Compared with the CO_2RR FEs of yolk–shell Cu@SnO_2 (88.8% at −1.05 V (*vs.* RHE)) and core–shell Cu@SnO_2 nanocatalysts (89.0% at −1.35 V), the Cu@SnO_2 nanocatalyst presented a superior FE_{CO} of 25.3% and a $FE_{formate}$ of 70.0%. The total FE of the CO_2RR was about 95.3% at −1.45 V (*vs.* RHE), as shown in Fig. 9h. It was suggested that the co-existence of thermodynamically stable fcc and unconventional hcp phases, together with abundant planar defects, in the multi-phase Cu core contributed to the outstanding CO_2RR performance.

5.3. Metal nanocatalysts with amorphous phase for the CO_2RR

While many reports have focused on crystalline nanocatalysts, metal nanomaterials with amorphous phase are becoming another promising candidate for the CO_2RR [125]. Compared to crystalline materials, amorphous materials generally have large amounts of under-coordinated and disordered atoms, which may provide more active sites for anchoring CO_2 atoms for subsequent conversion.

5.3.1. Amorphous metal nanocatalysts

As a typical example, amorphous Cu nanoparticles showed excellent performance towards the generation of C_{2+} liquid products during the CO_2RR [32]. As shown in Figs. 10a–c, the amorphous Cu nanoparticles presented a superior FE_{HCOOH} of 37% and a $FE_{C_2H_5OH}$ of 22% at −1.40 V (*vs.* Ag/AgCl). The total FE of the CO_2RR reached 59%. In comparison, the fcc Cu nanoparticles displayed a FE_{HCOOH} of only 26%. The amorphous structure could increase the active specific surface area and improve CO_2 adsorption ability for the CO_2RR [32]. In another example, Xu et al. reported the synthesis of amorphous Cu nanoparticles by dealloying from a Cu–Li solid solution [83]. It was found that Cu migration and aggregation were weak, so an atomically amorphous structure was formed, driving the CO_2RR for selectively producing C_2H_5OH with a high FE of 91% at −0.7 V (*vs.* RHE) (Fig. 10d). In addition, the amorphous metal nanocatalysts exhibited a wider voltage range with superior CO_2RR performance compared to their crystalline counterparts. Amorphous Bi and Sn nanomaterials are also attractive in the CO_2RR [78]. As another example, Zheng et al. designed sulfur-modulated Sn nanocatalyst with a uniform amorphous layer (2–3 nm) through an atomic layer deposition and subsequent electrochemical in situ reduction process (Figs. 10e and f) [30]. The Sn in the obtained amorphous Sn(S) nanomaterials showed higher oxidation states than that of Sn nanoparticles. The amorphous Sn-based nanocatalysts enabled highly selective electrochemical reduction of CO_2 to formate with a FE of 93% at −0.75 V (*vs.* RHE). The outstanding catalytic activity of formate production is ascribed to undercoordinated Sn sites in the amorphous Sn layer [117].

5.3.2. Metal nanocatalysts with amorphous/crystalline heterophase

Hybridizing the amorphous phase with other crystalline phases is also promising for realizing a highly efficient CO_2RR. For example, phase engineering of metal nanomaterials by phase transformation between amorphous and crystalline phases offers new opportunities for modulating reaction pathways and enhancing CO_2RR performance. Recently, Hu et al. reported the synthesis of amorphous CuTi alloys with coordinatively unsaturated Cu sites by a melting, spinning, and etching process (Fig. 10g) [84]. The designed nanocatalyst could drive the CO_2RR to produce C_{2-4} with an overall FE of 48.82% at −0.8 V (*vs.* RHE). It was suggested that the Ti atoms under the surface donate electrons, and the

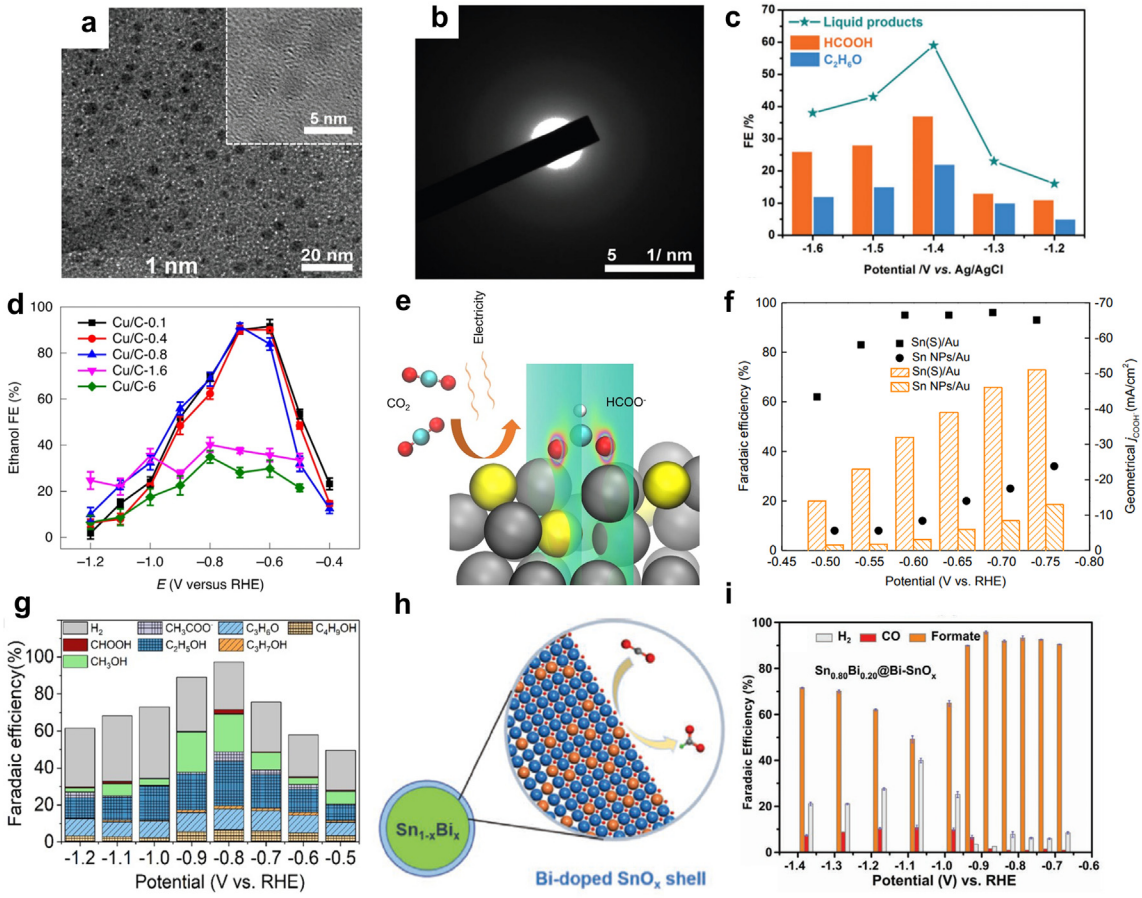

Fig. 10. (a) TEM image, (b) Selected Area Electron Diffraction (SAED) pattern, and (c) FEs of amorphous Cu nanoparticles for liquid products at given potentials between −1.2 and −1.5 V. Reproduced with permission from Ref. [32]. Copyright 2018, John Wiley & Sons, Inc. (d) FEs for C_2H_5OH formation at potentials between −0.4 and −1.2 V over Cu/C nanocatalysts with different Cu loadings. Reproduced with permission from Ref. [83]. Copyright 2020, Nature Publishing Group. (e) Reaction mechanism of the CO_2RR over Sn nanocatalysts with an amorphous layer. (f) Potential dependence (with iR corrected) of FEs and current densities for the CO_2RR on Sn(S)/Au (squares) and Sn NPs/Au (circles). Reproduced with permission from Ref. [30]. Copyright 2017, Cell Press. (g) FEs for the products of amorphous CuTi alloy electrocatalysts at different potentials. Reproduced with permission from Ref. [84]. Copyright 2021, John Wiley & Sons, Inc. (h) A structural model of Bi-doped SnO_x catalyst for the CO_2RR. (i) FEs for H_2, CO, and formate obtained on $Sn_{0.80}Bi_{0.20}$@Bi-SnO_x nanocatalysts. Reproduced with permission from Ref. [61]. Copyright 2020, John Wiley & Sons, Inc.

Cu active sites attain high oxygen affinity, which stabilizes intermediates on the nanocatalyst and enhances multi-carbon production.

In addition to Cu, Lum et al. constructed a PdAu dendritic nanocatalyst consisting of fcc Pd and amorphous Au on a glassy carbon electrode through an electrochemical deposition method [126]. The nanocatalysts with 3.2 at.% Au showed the highest FE towards ethylene glycol, 70%, through CO reduction. It was suggested that the addition of Au boosted the FE and partial current density towards ethylene glycol. Yang et al. reported unique amorphous Sn-based nanoshells on Sn–Bi alloy nanoparticles [61], which possessed high formate selectivity, with the maximum FE reaching 95.8% at −0.88 V (*vs.* RHE) and FEs above 91.5% in a wide potential range between −0.67 and −0.92 V (*vs.* RHE) (Figs. 10h and i). It was suggested that the Bi atoms allowed easier electron movement from Sn to Bi, thus reducing the energy barrier and boosting the charge transfer processes. Other types of amorphous Sn-based nanomaterials, such as In–Sn, Ag–Sn, and Cu–Sn nanostructures, have also been developed [127] (see Table 1).

6. Challenges and perspectives

This review summarizes the most recent developments in phase engineering of metal nanocatalysts towards the CO_2RR. First, various synthesis strategies for controlling the phase of metal nanocatalysts have been summarized, including the colloidal synthetic method, electrochemical method, heat treatment, and some others. Those methods illustrate the numerous advantages of using phase control with metal nanocatalysts to obtain unconventional phases (including an amorphous phase), crystallographic defects (including TBs and SFs), as well as various hetero-nanostructures. Second, distinct from size, composition, and architecture controls, phase control focuses on a new structural parameter and provides another powerful strategy to tune the catalytic properties of metal nanocatalysts. Crystal phase-dependent studies demonstrate the phase-dependent behaviors of metal nanocatalysts and therefore the uniqueness of PEN. These phase-engineered metal nanocatalysts show excellent performance, in terms of high activity, high selectivity, and wide potential window, towards a broad range of valuable products through adjusting their comparative binding strength towards CO_2 and intermediates in the electrocatalytic CO_2RR. In all, the exploration of novel synthetic methods for preparing metal nanocatalysts with unique phases and the investigation of their potential in the CO_2RR are intriguing and promising research directions.

Although great achievements have been made in the field of PEN for the electrochemical CO_2RR, many challenges remain. Firstly, it is still difficult to produce metal nanocatalysts with rationally designed phases at commercial scales to enable the future industrialization of CO_2RR electrocatalytic systems. Secondly, various surface ligands are unavoidably involved in colloidal synthesis processes for synthesizing metal nanocatalysts with novel phases. Different surface ligands play diverse

Table 1
Summary of representative metal nanocatalysts with conventional, unconventional, and amorphous phases towards the CO_2RR.

Crystal phase		Metal nanocatalysts	Synthetic strategy	CO_2RR main product @electrolyte (pH, if mentioned)	FE/potential	Stability	Ref.
Metal nanocatalysts with conventional phases	Transition metal nanocatalysts (excluding Cu)	Au needles	Electrodeposition	CO @ 0.5 M $KHCO_3$ (7.2)	95%/−0.35 V (*vs.* RHE)	−0.35 V (*vs.* RHE)/8 h	[100]
		Pd needles	Electrodeposition	Formate @ 0.5 M $KHCO_3$ (7.2)	91%/−0.20 V (*vs.* RHE)	−0.20 V (*vs.* RHE)/20 h	[100]
		Au quantum dot derived nanocatalysts	Colloidal synthesis followed by in situ electrochemical reduction	CO @ 0.5 M $KHCO_3$ (7.2)	~95%/−0.16 V (*vs.* RHE)	−0.30 V (*vs.* RHE)/80 h	[101]
		5-fold twinned Ag nanowires	Colloidal synthesis	CO @ 0.1 M $KHCO_3$	99.3%/−0.96 V (*vs.* RHE)	−0.86 V (*vs.* RHE)/24 h	[102]
		Ferromagnetic hcp Co nanosheet	Colloidal synthesis with exfoliation method	CH_3CHO @ 0.5 M $KHCO_3$	60%/−0.40 V (*vs.* RHE)	−0.40 V (*vs.* RHE)/100 h	[104]
		Partially oxidized Co nanosheets	Colloidal synthesis	Formate @ 0.1 M Na_2SO_4 (6)	90.1%/−0.85 V (*vs.* SCE)	−0.85 V (*vs.* SCE)/40 h	[105]
		Zn nanoparticles	Colloidal synthesis	CO @ 0.1 M $KHCO_3$	~70%/−1.10 V (*vs.* RHE)	/	[106]
		Hierarchical hcp Zn	Electrodeposition	CO @ 0.5 M $KHCO_3$	~85.4%/−0.95 V (*vs.* RHE)	−1.10 V (*vs.* RHE)/30 h	[107]
	Cu nanocatalysts	(111)-enclosed Cu nanosheets	Colloidal synthesis	C_{2+} products @ 2 M KOH Acetate @ 2 M KOH	70%/−0.60 V (*vs.* RHE) 48%/−0.75 V (*vs.* RHE)	−0.75 V (*vs.* RHE)/3 h	[112]
		Cu with exposed (100) facets	Electrodeposition	C_{2+} products @ 7 M KOH	90%/−0.67 V (*vs.* RHE)	full-cell voltage of −3.70 V/65 h	[113]
		Cu with twin TBs −16 nm	Electrodeposition	C_2H_4 @ 0.2 M $NaHCO_3$	59%/−1.60 V (*vs.* RHE)	/	[80]
		Star decahedron Cu nanoparticle with TBs	Colloidal synthesis	C_2H_4 @ 0.1 M $NaHCO_3$	52.43% ± 2.72% for C_2H_4 production at −0.993 ± 0.0129 V (*vs.* RHE)	−1.00 V (*vs.* RHE)/12 h	[51]
	Main group metal nanocatalysts	Bi nanocatalyst with rich grain boundaries (GBs)	Chemical lithium tuning method	Formate @ 0.5 M $KHCO_3$	~97%/−0.77 V (*vs.* RHE)	−0.77 V (*vs.* RHE)/100 h	[116]
		Mesoporous Bi nanosheets	Colloidal synthesis	Formate @ 0.5 M $KHCO_3$	~99%/−0.90 V (*vs.* RHE)	−0.08 V (*vs.* RHE)/12 h	[43]
		Sn nanosheets	Colloidal synthesis	Formate @ 0.1 M $NaHCO_3$	89%/−1.80 V (*vs.* SCE)	−1.80 V (*vs.* SCE)/50 h	[117]
	Bimetallic nanocatalysts	Lattice-dislocated Bi nanowires	Galvanic replacement method followed by in situ electrochemical reduction	Formate @ 0.5 M $KHCO_3$	95%/−0.70 V (*vs.* RHE)	−0.69 V (*vs.* RHE)/12 h	[121]
		Phase-separated CuPd	Colloidal synthesis	C_2 @ 1 M KOH	63%/−0.70 V (*vs.* RHE)	/	[46]
		Ag–Cu Janus nanostructures	Colloidal synthesis	C_{2+} @ 0.1 M $NaHCO_3$ C_2H_4 @ 0.1 M $NaHCO_3$	72%/−1.20 V (*vs.* RHE) 54%/−1.20 V (*vs.* RHE)	−1.20 V (*vs.* RHE)/10 h	[122]
Metal nanocatalysts with unconventional crystal phases	Au nanocatalysts with unconventional crystal phases	4H nanoribbons	Colloidal synthesis	CO @ 0.5 M $KHCO_3$	90%/−0.70 V (*vs.* RHE)	/	[33]
		4H/fcc Au nanorods	Colloidal synthesis	CO @ 0.5 M $KHCO_3$	90%/−0.70 V (*vs.* RHE)	/	[33]
		fcc-2H-fcc Au nanorods	Colloidal synthesis	CO @ 0.5 M $KHCO_3$	98.2%/−0.60 V (*vs.* RHE)	−0.60 V (*vs.* RHE)/24 h	[34]
		fcc-2H-fcc Pd@Au nanorods	Colloidal synthesis	CO @ 0.5 M $KHCO_3$	~98.7%/−0.50 V (*vs.* RHE)	−0.60 V (*vs.* RHE)/45 h	[35]
	Cu nanocatalysts with unconventional crystal phases	4H/fcc Au@Cu	Colloidal synthesis	Overall CO_2RR products/ C_2H_4 @ 0.1 M $KHCO_3$	~91%/−0.82 V (*vs.* RHE) 46.7%/−1.17 V (*vs.* RHE)	/	[36]
	Other metal nanocatalysts with unconventional crystal phases	fct $AuCu_3$@Au	Colloidal synthesis and heat treatment	CO @ 0.1 M $KHCO_3$	94.5%/−0.80 V (*vs.* RHE)	−0.80 V (*vs.* RHE)/20 h	[37]
		Orthorhombic intermetallic ε-phase $Ag_{76}Sn_{24}$ nanocatalyst	Colloidal synthesis	Formate @ 0.5 M $KHCO_3$	87.2%/−0.90 V (*vs.* RHE)	−0.80 V (*vs.* RHE)/24 h	[31]
		Cu with unconventional crystal phases (e.g., 2H, 4H, and 6H) @ amorphous SnO_2 shell	Colloidal synthesis	C_1 products (Formate/CO) @ 0.1 M $KHCO_3$	95.3% (70.0%/25.3%)/ −1.45 V (*vs.* RHE)	−1.05 V (*vs.* RHE)/12 h	[38]

(*continued on next page*)

Table 1 (*continued*)

Crystal phase		Metal nanocatalysts	Synthetic strategy	CO_2RR main product @electrolyte (pH, if mentioned)	FE/potential	Stability	Ref.
Metal nanocatalysts with amorphous phases	Amorphous metal nanocatalysts	Amorphous Cu nanoparticles	Colloidal synthesis	HCOOH and C_2H_5OH @ 0.1 M $KHCO_3$	59%/−1.40 V (*vs.* Ag/AgCl)	−1.40 V (*vs.* RHE)/12 h	[32]
		Amorphous Cu nanoparticles from Cu–Li solid solution	Amalgamated Cu–Li method	C_2H_5OH @ 0.1 M $KHCO_3$	91%/−0.70 V (*vs.* RHE)	−0.40 V (*vs.* RHE)/16 h	[83]
		Disordered Ag nanoparticles	Colloidal synthesis	CO @ 0.1 M $KHCO_3$	90%/(−0.60 ~ −1.70 V) (*vs.* RHE)	−0.75 V (*vs.* RHE)/60 h	[29]
		Sn nanocatalyst with a uniform amorphous layer	Atomic layer deposition	Formate @ 0.1 M $KHCO_3$	93%/−0.75 V (*vs.* RHE)	−0.75 V (*vs.* RHE)/40 h	[30]
	Metal nanocatalysts with amorphous/crystalline heterophases	Amorphous phase of CuTi	Alloying–dealloying method	C_{2-4} alcohols and ketones @ 0.1 M $KHCO_3$	48.82%/−0.80 V (*vs.* RHE)	−0.80 V (*vs.* RHE)/3 month/49%	[84]
		Bi-Sn crystalline/amorphous heterophase structure	Colloidal synthesis	Formate @ 0.5 M $KHCO_3$	95.8%/−0.88 V (*vs.* RHE)	−0.02 V (*vs.* RHE)/50 h	[62]
		$SnInO_X$ films	Thermal decomposition	Formate @ 0.1 M $KHCO_3$	80%/−1.00 V (*vs.* RHE)	−1.00 V (*vs.* RHE)/10 h	[127]

roles in influencing catalytic performance. For example, some surface ligands may inhibit or facilitate mass transfer processes during the CO_2RR [128,129], while some may affect the adsorption of CO_2 or intermediates [130], making it more difficult to distinguish the effect of phases. Thirdly, comprehensive mechanistic studies and theoretical explanations of the formation of unconventional phases, heterophases, and crystallographic defects via various synthetic methods are still lacking. Plus, developing a novel PEN method to prepare nanocatalysts without surface ligands is still a great challenge. This could possibly be realized by using high-temperature shockwave methods that have been used for preparing high-entropy metal nanoalloys [131,132]. In addition, a more comprehensive investigation of the phase-dependent catalytic performance (e.g., selectivity, activity, and stability) in the CO_2RR is still desired. Although the reaction mechanisms of the CO_2RR have been studied in some reports, we still lack direct evidence of the catalytic mechanisms with conventional and unconventional phases of metals to establish the structure–property relationship. One possible approach is to monitor the reaction intermediates by applying in situ characterization techniques such as in situ X-ray absorption spectroscopy, in situ Fourier transform infrared spectroscopy [133], and in situ Raman spectroscopy [134]; in this way, information on the adsorption/desorption profiles of reaction intermediates during the CO_2RR could be obtained, verifying the proposed reaction pathways, which could, in turn, guide nanocatalyst design and synthesis. Lastly, as a prerequisite for the CO_2RR, the stability of the novel phases of nanocatalysts during electrocatalysis should be well understood and enhanced. In situ observation tools such as in situ TEM could be employed to obtain mechanistic insights into the phase transformation of metal nanocatalysts during the CO_2RR, if any. Furthermore, the fast development in high-throughput calculation may bring further opportunities to screen for better metal-based CO_2RR electrocatalysts with pre-designed phases [135]. The correlation between key performance descriptors, such as adsorption energies, d-band center, as well as coordination number, and the phases of metal nanocatalysts may be predicted to guide more efficient catalyst design.

In summary, there are many unexplored directions and great opportunities in the area of PEN for the electrochemical CO_2RR. It is believed that further progress in this promising field will motivate innovations in the rational design and synthesis of novel nanocatalysts, especially with unconventional phases, as well as the future development of metal-based systems on a commercial scale.

Author contributions

X. Zhang, Y. Chen, and H. Zhang proposed the concept. Y. J. Zhai and P. Han co-wrote the manuscript. All authors revised the manuscript.

Declaration of competing interest

The authors declare no competing financial interests.

Acknowledgments

X. Z. acknowledges the support from the Start-up Fund (BDC2) and Research Institute for Advanced Manufacturing (RIAM) Fund (CD4D) from the Hong Kong Polytechnic University. Y. C. thanks the support from Start-up Fund (Project No. 4930977), the Direct Grant for Research (Project No. 4053444) from the Chinese University of Hong Kong. H. Z. thanks the support from ITC via the Hong Kong Branch of National Precious Metals Material Engineering Research Center (NPMM), the Research Grants Council of Hong Kong (GRF Project No. 11301721), the Start-Up Grant (Project No. 9380100) and the grants (Project Nos. 7020054, 9678272, and 1886921) from the City University of Hong Kong, the Science Technology and Innovation Committee of Shenzhen Municipality ("Preparation of single atoms on transition metal chalcogenides for electrolytic hydrogen evolution", CityU), and the Project 52131301 supported by NSFC.

References

[1] X.Y. Tan, C. Yu, Y.W. Ren, S. Cui, W.B. Li, J.S. Qiu, Recent advances in innovative strategies for the CO_2 electroreduction reaction, Energy Environ. Sci. 14 (2021) 765–780.

[2] R. Daiyan, W.H. Saputera, H. Masood, J. Leverett, X.Y. Lu, R. Amal, A Disquisition on the active sites of heterogeneous catalysts for electrochemical reduction of CO_2 to value-added chemicals and fuel, Adv. Energy Mater. 10 (2020) 1902106.

[3] S. Chu, Y. Cui, N. Liu, The path towards sustainable energy, Nat. Mater. 16 (2017) 16–22.

[4] A. Rafiee, K.R. Khalilpour, D. Milani, M. Panahi, Trends in CO_2 conversion and utilization: a review from process systems perspective, J. Environ. Chem. Eng. 6 (2018) 5771–5794.

[5] Y. Zhang, S.X. Guo, X.L. Zhang, A.M. Bond, J. Zhang, Mechanistic understanding of the electrocatalytic CO_2 reduction reaction-new developments based on advanced instrumental techniques, Nano Today 31 (2020) 100835.

[6] J. Su, Y. Liu, Y. Song, L. Huang, W. Guo, X. Cao, Y. Dou, L. Cheng, G. Li, Q. Hu, Recent development of nanomaterials for carbon dioxide electroreduction, SmartMat 3 (2022) 35–53.

[7] J.J. Wang, X.P. Li, B.F. Cui, Z. Zhang, X.F. Hu, J. Ding, Y.D. Deng, X.P. Han, W.B. Hu, A review of non-noble metal-based electrocatalysts for CO_2 electroreduction, Rare Metals 40 (2021) 3019–3037.

[8] X. Huang, J.L. Song, M.L. Hua, Z.B. Xie, S.S. Liu, T.B. Wu, G.Y. Yang, B.X. Han, Enhancing the electrocatalytic activity of CoO for the oxidation of 5-hydroxymethylfurfural by introducing oxygen vacancies, Green Chem. 22 (2020) 843–849.

[9] J.J. Wang, G.J. Wang, J.F. Zhang, Y.D. Wang, H. Wu, X.R. Zheng, J. Ding, X.P. Han, Y.D. Deng, W.B. Hu, Inversely tuning the CO_2 electroreduction and hydrogen evolution activity on metal oxide via heteroatom doping, Angew. Chem. Int. Ed. 133 (2021) 7680–7684.

[10] M.H. Li, H.F. Wang, W. Luo, P.C. Sherrell, J. Chen, J.P. Yang, Heterogeneous single-atom catalysts for electrochemical CO_2 reduction reaction, Adv. Mater. 32 (2020) 2001848.

[11] D.F. Gao, T.F. Liu, G.X. Wang, X.H. Bao, Structure sensitivity in single-atom catalysis toward CO_2 electroreduction, ACS Energy Lett. 6 (2021) 713–727.

[12] S. Liu, H.B. Yang, S.F. Hung, J. Ding, W.Z. Cai, L.H. Liu, J.J. Gao, X.N. Li, X.Y. Ren, Z.C. Kuang, Elucidating the electrocatalytic CO_2 reduction reaction over a model single-atom nickel catalyst, Angew. Chem. Int. Ed. 59 (2020) 798–803.

[13] D.H. Nam, O.S. Bushuyev, J. Li, P. De Luna, A. Seifitokaldani, C.T. Dinh, F.P. García de Arquer, Y.H. Wang, Z.Q. Liang, A.H. Proppe, Metal-organic frameworks mediate Cu coordination for selective CO_2 electroreduction, J. Am. Chem. Soc. 140 (2018) 11378–11386.

[14] D. Yang, X. Wang, 2D π-conjugated metal-organic frameworks for CO_2 electroreduction, SmartMat 3 (2022) 54–67.

[15] X. Yang, Q.X. Li, S.Y. Chi, H.F. Li, Y.B. Huang, R. Cao, Hydrophobic perfluoroalkane modified metal-organic frameworks for the enhanced electrocatalytic reduction of CO_2, SmartMat 3 (2022) 163–172.

[16] M. Asadi, K. Kim, C. Liu, A.V. Addepalli, P. Abbasi, P. Yasaei, P. Phillips, A. Behranginia, J.M. Cerrato, R. Haasch, Nanostructured transition metal dichalcogenide electrocatalysts for CO_2 reduction in ionic liquid, Science 353 (2016) 467–470.

[17] M. Asadi, B. Kumar, A. Behranginia, B.A. Rosen, A. Baskin, N. Repnin, D. Pisasale, P. Phillips, W. Zhu, R. Haasch, Robust carbon dioxide reduction on molybdenum disulphide edges, Nat. Commun. 5 (2014) 1–8.

[18] C. Chang, W. Chen, Y. Chen, et al., Recent progress on two-dimensional materials, Acta Phys. Chim. Sin. 37 (2021) 2108017.

[19] Z.W. Seh, J. Kibsgaard, C.F. Dickens, I. Chorkendorff, J.K. Norskov, T.F. Jaramillo, Combining theory and experiment in electrocatalysis: insights into materials design, Science 355 (2017) eaad4998.

[20] S.R. Hui, P. De Luna, How increasing proton and electron conduction benefits electrocatalytic CO_2 reduction, Matter 4 (2021) 1555–1577.

[21] S.L. Jiao, X.W. Fu, H.W. Huang, Descriptors for the evaluation of electrocatalytic reactions: d-band theory and beyond, Adv. Funct. Mater. 32 (2021) 2107651.

[22] Y.Y. Birdja, E. Pérez-Gallent, M.C. Figueiredo, A.J. Göttle, F. Calle-Vallejo, M.T.M. Koper, Advances and challenges in understanding the electrocatalytic conversion of carbon dioxide to fuels, Nat. Energy 4 (2019) 732–745.

[23] A.Q. Chen, B.L. Lin, A simple framework for quantifying electrochemical CO_2 fixation, Joule 2 (2018) 594–606.

[24] D.M. Koshy, S.A. Akhade, A. Shugar, K. Abiose, J.W. Shi, S. Liang, J.S. Oakdale, S.E. Weitzner, J.B. Varley, E.B. Duoss, S.E. Baker, C. Hahn, Z. Bao, T.F. Jaramillo, Chemical modifications of Ag catalyst surfaces with imidazolium ionomers modulate H_2 evolution rates during electrochemical CO_2 reduction, J. Am. Chem. Soc. 143 (2021) 14712–14725.

[25] J.J. Fu, W.L. Zhu, Y. Chen, Z.Y. Yin, Y.Y. Li, J. Liu, H.Y. Zhang, J.J. Zhu, S.H. Sun, Bipyridine-assisted assembly of Au nanoparticles on Cu nanowires to enhance the electrochemical reduction of CO_2, Angew. Chem. Int. Ed. 131 (2019) 14238–14241.

[26] Q. Chang, J. Kim, J.H. Lee, S. Kattel, J.G. Chen, S.I. Choi, Z. Chen, Boosting activity and selectivity of CO_2 electroreduction by pre-hydridizing Pd nanocubes, Small 16 (2020) e2005305.

[27] H. Xie, T.Y. Wang, J.S. Liang, Q. Li, S.H. Sun, Cu-based nanocatalysts for electrochemical reduction of CO_2, Nano Today 21 (2018) 41–54.

[28] Y. Chen, Z.C. Lai, X. Zhang, Z.X. Fan, Q.Y. He, C.L. Tan, H. Zhang, Phase engineering of nanomaterials, Nat. Rev. Chem. 4 (2020) 243–256.

[29] W.Y. Deng, L. Zhang, H. Dong, X.X. Chang, T. Wang, J.L. Gong, Achieving convenient CO_2 electroreduction and photovoltage in tandem using potential-insensitive disordered Ag nanoparticles, Chem. Sci. 9 (2018) 6599–6604.

[30] X.L. Zheng, P. De Luna, F.P.G. de Arquer, B. Zhang, N. Becknell, M.B. Ross, Y. Li, M.N. Banis, Y.Z. Li, M. Liu, O. Voznyy, C.T. Dinh, T. Zhuang, P. Stadler, Y. Cui, X. Du, P. Yang, E.H. Sargent, Sulfur-modulated tin sites enable highly selective electrochemical reduction of CO_2 to formate, Joule 1 (2017) 794–805.

[31] W. Luc, C. Collins, S.W. Wang, H.L. Xin, K. He, Y.J. Kang, F. Jiao, Ag-Sn bimetallic catalyst with a core-shell structure for CO_2 reduction, J. Am. Chem. Soc. 139 (2017) 1885–1893.

[32] Y.X. Duan, F.L. Meng, K.H. Liu, S.S. Yi, S.J. Li, J.M. Yan, Q. Jiang, Amorphizing of Cu nanoparticles toward highly efficient and robust electrocatalyst for CO_2 reduction to liquid fuels with high Faradaic efficiencies, Adv. Mater. 30 (2018) e1706194.

[33] Y.X. Wang, C.Y. Li, Z.X. Fan, Y. Chen, X. Li, L. Cao, C.H. Wang, L. Wang, D. Su, H. Zhang, T. Mueller, C. Wang, Undercoordinated active sites on 4H gold nanostructures for CO_2 reduction, Nano Lett. 20 (2020) 8074–8080.

[34] Z.X. Fan, M. Bosman, Z.Q. Huang, Y. Chen, C.Y. Ling, L. Wu, Y.A. Akimov, R. Laskowski, B. Chen, P. Ercius, J. Zhang, X.Y. Qi, M.H. Goh, Y.Y. Ge, Z.C. Zhang, W. Niu, J.L. Wang, H.M. Zheng, H. Zhang, Heterophase fcc-2H-fcc gold nanorods, Nat. Commun. 11 (2020) 3293.

[35] Y.Y. Ge, Z.Q. Huang, C.Y. Ling, B. Chen, G.G. Liu, M. Zhou, J.W. Liu, X. Zhang, H.F. Cheng, G.H. Liu, Y.H. Du, C.J. Sun, C.L. Tan, J.T. Huang, P.F. Yin, Z.X. Fan, Y. Chen, N.L. Yang, H. Zhang, Phase-selective epitaxial growth of heterophase nanostructures on unconventional 2H-Pd nanoparticles, J. Am. Chem. Soc. 142 (2020) 18971–18980.

[36] Y. Chen, Z.X. Fan, J. Wang, C.Y. Ling, W.X. Niu, Z.Q. Huang, G.G. Liu, B. Chen, Z.C. Lai, X.Z. Liu, B. Li, Y. Zong, L. Gu, J.L. Wang, X. Wang, H. Zhang, Ethylene selectivity in electrocatalytic CO_2 reduction on Cu nanomaterials: a crystal phase-dependent study, J. Am. Chem. Soc. 142 (2020) 12760–12766.

[37] D. Yu, L. Gao, T.L. Sun, J.C. Guo, Y.L. Yuan, J.W. Zhang, M.F. Li, X.X. Li, M.C. Liu, C. Ma, Q.H. Liu, A.L. Pan, J.L. Yang, H.W. Huang, Strain-stabilized metastable face-centered tetragonal gold overlayer for efficient CO_2 electroreduction, Nano Lett. 21 (2021) 1003–1010.

[38] P.F. Yin, J.J. Fu, Q.B. Yun, B. Chen, G.G. Liu, L.J. Li, Z.Q. Huang, Y.Y. Ge, H. Zhang, Preparation of amorphous SnO_2-encapsulated multi-phased crystalline Cu heterostructures for highly efficient CO_2 reduction, Adv. Mater. 34 (2022) 2201114.

[39] N. Han, P. Ding, L. He, Y.Y. Li, Y.G. Li, Promises of main group metal-based nanostructured materials for electrochemical CO_2 reduction to formate, Adv. Energy Mater. 10 (2019) 1902338.

[40] S. Jin, Z. Hao, K. Zhang, Z. Yan, J. Chen, Advances and challenges for the electrochemical reduction of CO_2 to CO: from fundamentals to industrialization, Angew. Chem. Int. Ed. 60 (2021) 20627–20648.

[41] Y. Wang, J. Liu, G. Zheng, Designing copper-based catalysts for efficient carbon dioxide electroreduction, Adv. Mater. 33 (2021) e2005798.

[42] Y. Zhao, J.J. Liang, C.Y. Wang, J.M. Ma, G.G. Wallace, Tunable and efficient Tin modified nitrogen-doped carbon nanofibers for electrochemical reduction of aqueous carbon dioxide, Adv. Energy Mater. 8 (2018) 1702524.

[43] H. Yang, N. Han, J. Deng, J.H. Wu, Y. Wang, Y.P. Hu, P. Ding, Y.F. Li, Y.G. Li, J. Lu, Selective CO_2 reduction on 2D mesoporous Bi nanosheets, Adv. Energy Mater. 8 (2018) 1801536.

[44] X. Huang, S. Li, Y. Huang, S. Wu, X. Zhou, S. Li, C.L. Gan, F. Boey, C.A. Mirkin, H. Zhang, Synthesis of hexagonal close-packed gold nanostructures, Nat. Commun. 2 (2011) 292.

[45] Z.X. Fan, M. Bosman, X. Huang, D. Huang, Y. Yu, K.P. Ong, Y.A. Akimov, L. Wu, B. Li, J. Wu, Y. Huang, Q. Liu, C. Eng Png, C. Lip Gan, P.D. Yang, H. Zhang, Stabilization of 4H hexagonal phase in gold nanoribbons, Nat. Commun. 6 (2015) 7684.

[46] S. Ma, M. Sadakiyo, M. Heima, R. Luo, R.T. Haasch, J.I. Gold, M. Yamauchi, P.J. Kenis, Electroreduction of carbon dioxide to hydrocarbons using bimetallic Cu-Pd catalysts with different mixing patterns, J. Am. Chem. Soc. 139 (2017) 47–50.

[47] J.Z. Liang, Y.Y. Ge, Z. He, Q.B. Yun, G.G. Liu, S.Y. Lu, L. Zhai, B. Huang, H. Zhang, Wet-chemical synthesis and applications of amorphous metal-containing nanomaterials, Nano Res. 20 (2021) 1–21.

[48] K. Lu, L. Lu, S. Suresh, Strengthening materials by engineering coherent internal boundaries at the nanoscale, Science 324 (2009) 349–352.

[49] K. Lu, Stabilizing nanostructures in metals using grain and twin boundary architectures, Nat. Rev. Mater. 1 (2016) 1–13.

[50] J.W. Wang, S. Narayanan, J.Y. Huang, Z. Zhang, T. Zhu, S.X. Mao, Atomic-scale dynamic process of deformation-induced stacking fault tetrahedra in gold nanocrystals, Nat. Commun. 4 (2013) 2340.

[51] C. Choi, T. Cheng, M. Flores Espinosa, H. Fei, X. Duan, W.A. Goddard, Y. Huang, A highly active star decahedron Cu nanocatalyst for hydrocarbon production at low overpotentials, Adv. Mater. 31 (2019) 1805405.

[52] F. Hu, S.C. Abeyweera, J. Yu, D. Zhang, Y. Wang, Q.M. Yan, Y.G. Sun, Quantifying electrocatalytic reduction of CO_2 on twin boundaries, Chem 6 (2020) 3007–3021.

[53] S.Y. Zhao, A.H. Liu, Y.H. Li, Y.Y. Wen, X.Q. Gao, Q.L. Chen, Boosting the electrocatalytic CO_2 reduction reaction by nanostructured metal materials via defects engineering, Nanomaterials 12 (2022) 2389.

[54] A.R. Tao, S. Habas, P.D. Yang, Shape control of colloidal metal nanocrystals, Small 4 (2008) 310–325.

[55] X.H. Ji, X.N. Song, J. Li, Y.B. Bai, W.S. Yang, X.G. Peng, Size control of gold nanocrystals in citrate reduction: the third role of citrate, J. Am. Chem. Soc. 129 (2007) 13939–13948.

[56] J. Liu, J.T. Huang, W.X. Niu, C.L. Tan, H. Zhang, Unconventional-phase crystalline materials constructed from multiscale building blocks, Chem. Rev. 121 (2021) 5830–5888.

[57] H.F. Cheng, N.L. Yang, Q.P. Lu, Z.C. Zhang, H. Zhang, Syntheses and properties of metal nanomaterials with novel crystal phases, Adv. Mater. 30 (2018) e1707189.

[58] G. Wang, C. Ma, L. Zheng, Y. Chen, Colloidal synthesis of Au nanomaterials with a controlled morphology and crystal phase via the [Au(i)-oleylamine] complex, J. Mater. Chem. A 9 (2021) 19534–19553.

[59] R.R. da Silva, M. Yang, S.I. Choi, M. Chi, M. Luo, C. Zhang, Z.Y. Li, P.H. Camargo, S.J. Ribeiro, Y. Xia, Facile synthesis of sub-20 nm silver nanowires through a bromide-mediated polyol method, ACS Nano 10 (2016) 7892–7900.

[60] Y. Chen, Z. Fan, Z. Luo, X. Liu, Z. Lai, B. Li, Y. Zong, L. Gu, H. Zhang, High-yield synthesis of crystal-phase-heterostructured 4H/fcc Au@Pd core-shell nanorods for electrocatalytic ethanol oxidation, Adv. Mater. 29 (2017) 1701331.

[61] Q. Yang, Q.L. Wu, Y. Liu, S.P. Luo, X.T. Wu, X.X. Zhao, H.Y. Zou, B.H. Long, W. Chen, Y.J. Liao, L.X. Li, P.K. Shen, L.L. Duan, Z.W. Quan, Novel Bi-doped amorphous SnO_x nanoshells for efficient electrochemical CO_2 reduction into formate at low overpotentials, Adv. Mater. 32 (2020) e2002822.

[62] M.B. Kale, R.A. Borse, A. Gomaa Abdelkader Mohamed, Y. Wang, Electrocatalysts by electrodeposition: recent advances, synthesis methods, and applications in energy conversion, Adv. Funct. Mater. 31 (2021) 2101313.

[63] W.W. Quan, Y.B. Lin, Y.J. Luo, Y.Y. Huang, Electrochemical CO_2 reduction on Cu: synthesis-controlled structure preference and selectivity, Adv. Sci. 8 (2021) e2101597.

[64] J. Medina-Ramos, R.C. Pupillo, T.P. Keane, J.L. DiMeglio, J. Rosenthal, Efficient conversion of CO_2 to CO using tin and other inexpensive and easily prepared post-transition metal catalysts, J. Am. Chem. Soc. 137 (2015) 5021–5027.

[65] L. Han, B.Q. Tian, X.X. Gao, Y. Zhong, S.N. Wang, S.C. Song, Z.L. Wang, Y. Zhang, Y. Kuang, X. Sun, Copper nanowire with enriched high-index facets for highly selective CO_2 reduction, SmartMat 3 (2022) 142–150.

[66] N. Tian, Z.Y. Zhou, S.G. Sun, Y. Ding, L. Wang Zhong, Synthesis of tetrahexahedral platinum nanocrystals with high-index facets and high electro-oxidation activity, Science 316 (2007) 732–735.

[67] C. Xiao, B.A. Lu, P. Xue, N. Tian, Z.Y. Zhou, X. Lin, W.F. Lin, S.G. Sun, High-index-facet- and high-surface-energy nanocrystals of metals and metal oxides as highly efficient catalysts, Joule 4 (2020) 2562–2598.

[68] L. Gao, X. Cui, C.D. Sewell, J. Li, Z. Lin, Recent advances in activating surface reconstruction for the high-efficiency oxygen evolution reaction, Chem. Soc. Rev. 50 (2021) 8428–8469.

[69] F.M. Liu, L. Zhang, L. Wang, F.Y. Cheng, The electrochemical tuning of transition metal-based materials for electrocatalysis, Electrochem. Energy Rev. 4 (2021) 146–168.

[70] Z. Lu, K. Jiang, G.X. Chen, H.T. Wang, Y. Cui, Lithium electrochemical tuning for electrocatalysis, Adv. Mater. 30 (2018) e1800978.

[71] S. Lee, G. Nam, J. Sun, J.S. Lee, H.W. Lee, W. Chen, J. Cho, Y. Cui, Enhanced intrinsic catalytic activity of λ-MnO_2 by electrochemical tuning and oxygen vacancy generation, Angew. Chem. Int. Ed. 55 (2016) 8741–8746.

[72] H.T. Wang, S.C. Xu, C. Tsai, Y.Z. Li, C. Liu, J. Zhao, Y.Y. Liu, H.Y. Yuan, F. Abild-Pedersen, B. Prinz Fritz, K. Nørskov Jens, Y. Cui, Direct and continuous strain control of catalysts with tunable battery electrode materials, Science 354 (2016) 1031–1036.

[73] Y.W. Lum, J.W. Ager, Evidence for product-specific active sites on oxide-derived Cu catalysts for electrochemical CO_2 reduction, Nat. Catal. 2 (2018) 86–93.

[74] D. Ren, Y.L. Deng, A.D. Handoko, C.S. Chen, S. Malkhandi, B.S. Yeo, Selective electrochemical reduction of carbon dioxide to ethylene and ethanol on copper(I) oxide catalysts, ACS Catal. 5 (2015) 2814–2821.

[75] W.C. Sheng, S. Kattel, S.Y. Yao, B.H. Yan, Z.X. Liang, C.J. Hawxhurst, Q.Y. Wu, J.G. Chen, Electrochemical reduction of CO_2 to synthesis gas with controlled CO/H_2 ratios, Energy Environ. Sci. 10 (2017) 1180–1185.

[76] D.F. Gao, H. Zhou, F. Cai, D.N. Wang, Y.F. Hu, B. Jiang, W.B. Cai, X.Q. Chen, R. Si, F. Yang, S. Miao, J.G. Wang, G.X. Wang, X.H. Bao, Switchable CO_2 electroreduction via engineering active phases of Pd nanoparticles, Nano Res. 10 (2017) 2181–2191.

[77] Y. Zhao, X. Tan, W.F. Yang, C. Jia, X.J. Chen, W.H. Ren, S.C. Smith, C. Zhao, Surface reconstruction of ultrathin palladium nanosheets during electrocatalytic CO_2 Reduction, Angew. Chem. Int. Ed. 59 (2020) 21493–21498.

[78] J. Medina-Ramos, J.L. DiMeglio, J. Rosenthal, Efficient reduction of CO_2 to CO with high current density using in situ or ex situ prepared Bi-based materials, J. Am. Chem. Soc. 136 (2014) 8361–8367.

[79] Z.B. Hoffman, T.S. Gray, K.B. Moraveck, T.B. Gunnoe, G. Zangari, Electrochemical reduction of carbon dioxide to syngas and formate at dendritic copper-indium electrocatalysts, ACS Catal. 7 (2017) 5381–5390.

[80] C. Tang, J.J. Shi, X.W. Bai, A.Q. Hu, N.N. Xuan, Y.W. Yue, T. Ye, B. Liu, P.X. Li, P.Y. Zhuang, J.F. Shen, Y.Y. Liu, Z.Z. Sun, CO_2 reduction on copper's twin boundary, ACS Catal. 10 (2020) 2026–2032.

[81] D. Kim, C. Xie, N. Becknell, Y. Yu, M. Karamad, K. Chan, E.J. Crumlin, J.K. Norskov, P. Yang, Electrochemical activation of CO_2 through atomic ordering transformations of AuCu nanoparticles, J. Am. Chem. Soc. 139 (2017) 8329–8336.

[82] L. Jia, M.Z. Sun, J. Xu, X. Zhao, R. Zhou, B.B. Pan, L. Wang, N. Han, B.L. Huang, Y.G. Li, Phase-dependent electrocatalytic CO_2 reduction on Pd_3Bi nanocrystals, Angew. Chem. Int. Ed. 133 (2021) 21909–21913.

[83] H.P. Xu, D. Rebollar, H.Y. He, L. Chong, Y.Z. Liu, C. Liu, C.J. Sun, T. Li, J.V. Muntean, R.E. Winans, D.J. Liu, T. Xu, Highly selective electrocatalytic CO_2 reduction to ethanol by metallic clusters dynamically formed from atomically dispersed copper, Nat. Energy 5 (2020) 623–632.

[84] F. Hu, L. Yang, Y.W. Jiang, C.X. Duan, X.N. Wang, L.J. Zeng, X.F. Lv, D.L. Duan, Q. Liu, T.T. Kong, J. Jiang, R. Long, Y.J. Xiong, Ultrastable Cu catalyst for CO_2 electroreduction to multicarbon liquid fuels by tuning C-C coupling with CuTi subsurface, Angew. Chem. Int. Ed. 60 (2021) 26122–26127.

[85] G.M. Tomboc, S. Choi, T. Kwon, Y.J. Hwang, K. Lee, Potential link between Cu surface and selective CO_2 electroreduction: perspective on future electrocatalyst designs, Adv. Mater. 32 (2020) 1908398.

[86] L.M. Wang, W.L. Chen, D.D. Zhang, Y.P. Du, R. Amal, S.Z. Qiao, J.B. Wu, Z.Y. Yin, Surface strategies for catalytic CO_2 reduction: from two-dimensional materials to nanoclusters to single atoms, Chem. Soc. Rev. 48 (2019) 5310–5349.

[87] T.K. Todorova, M.W. Schreiber, M. Fontecave, Mechanistic understanding of CO_2 reduction reaction (CO_2RR) toward multicarbon products by heterogeneous copper-based catalysts, ACS Catal. 10 (2019) 1754–1768.

[88] X. Zhi, A. Vasileff, Y. Zheng, Y. Jiao, S.Z. Qiao, Role of oxygen-bound reaction intermediates in selective electrochemical CO_2 reduction, Energy Environ. Sci. 14 (2021) 3912–3930.

[89] A. Vasileff, C.C. Xu, Y. Jiao, Y. Zheng, S.Z. Qiao, Surface and interface engineering in copper-based bimetallic materials for selective CO_2 electroreduction, Chem 4 (2018) 1809–1831.

[90] C. Shi, H.A. Hansen, A.C. Lausche, J.K. Nørskov, Trends in electrochemical CO_2 reduction activity for open and close-packed metal surfaces, Phys. Chem. Chem. Phys. 16 (2014) 4720–4727.

[91] Z. Yin, G.T.R. Palmore, S. Sun, Electrochemical reduction of CO_2 catalyzed by metal nanocatalysts, Trends Chem. 1 (2019) 739–750.

[92] J. Li, Z.Y. Wang, C. McCallum, Y. Xu, F.W. Li, Y.H. Wang, C.M. Gabardo, C.T. Dinh, T.T. Zhuang, L. Wang, Constraining CO coverage on copper promotes high-efficiency ethylene electroproduction, Nat. Catal. 2 (2019) 1124–1131.

[93] T.T. Zhuang, Y.J. Pang, Z.Q. Liang, Z.Y. Wang, Y. Li, C.S. Tan, J. Li, C.T. Dinh, P. De Luna, P.L. Hsieh, Copper nanocavities confine intermediates for efficient electrosynthesis of C_3 alcohol fuels from carbon monoxide, Nat. Catal. 1 (2018) 946–951.

[94] C. Kim, F. Dionigi, V. Beermann, X. Wang, T. Möller, P. Strasser, Alloy nanocatalysts for the electrochemical oxygen reduction (ORR) and the direct electrochemical carbon dioxide reduction reaction (CO_2RR), Adv. Mater. 31 (2019) 1805617.

[95] Y. Hori, A. Murata, R. Takahashi, Formation of hydrocarbons in the electrochemical reduction of carbon dioxide at a copper electrode in aqueous solution, J. Chem. Soc., Faraday Trans. 85 (1989) 2309–2326.

[96] C. Sow, G. Mettela, G.U. Kulkarni, Noble metal nanomaterials with nontraditional crystal structures, Annu. Rev. Mater. Sci. 50 (2020) 345–370.

[97] H.X. Li, X.C. Zhou, W. Zhai, S.Y. Lu, J.Z. Liang, Z. He, H.W. Long, T.F. Xiong, H.Y. Sun, Q.Y. He, Z.X. Fan, H. Zhang, Phase engineering of nanomaterials for clean energy and catalytic applications, Adv. Energy Mater. 10 (2020) 2002019.

[98] S. Dou, X. Wang, S. Wang, Rational design of transition metal-based materials for highly efficient electrocatalysis, Small Methods 3 (2019) 1800211.

[99] J. Kim, J.T. Song, H. Ryoo, J.G. Kim, S.Y. Chung, J. Oh, Morphology-controlled Au nanostructures for efficient and selective electrochemical CO_2 reduction, J. Mater. Chem. A 6 (2018) 5119–5128.

[100] M. Liu, Y.J. Pang, B. Zhang, P. De Luna, O. Voznyy, J. Xu, X.L. Zheng, C.T. Dinh, F.J. Fan, C.H. Cao, F.P.G. De Arquer, T.S. Safaei, A. Mepham, A. Klinkova, E. Kumacheva, T. Fillete, D. Sinton, S.O. Kelley, E.H. Sargent, Enhanced electrocatalytic CO_2 reduction via field-induced reagent concentration, Nature 537 (2016) 382–386.

[101] M. Liu, M.X. Liu, X.M. Wang, S.M. Kozlov, Z. Cao, P. De Luna, H.M. Li, X.Q. Qiu, K. Liu, J.H. Hu, Quantum-dot-derived catalysts for CO_2 reduction reaction, Joule 3 (2019) 1703–1718.

[102] S.B. Liu, Z. Wang, H.B. Tao, T.F. Li, Q. Liu, Z.H. Xu, X.Z. Fu, J.L. Luo, Ultrathin 5-fold twinned sub-25 nm silver nanowires enable highly selective electroreduction of CO_2 to CO, Nano Energy 45 (2018) 456–462.

[103] M. Usman, M. Humayun, M.D. Garba, L. Ullah, Z. Zeb, A. Helal, M.H. Suliman, B.Y. Alfaifi, N. Iqbal, M. Abdinejad, Electrochemical reduction of CO_2: a review of cobalt based catalysts for carbon dioxide conversion to fuels, Nanomaterials 11 (2021) 2029.

[104] J. Yin, Z.Y. Yin, J. Jin, M.Z. Sun, B.L. Huang, H.H. Lin, Z.H. Ma, M. Muzzio, M.Q. Shen, C. Yu, C.T. Dinh, H. Zhang, Y. Peng, p. Xi, C.H. Yan, S. Sun, A new hexagonal cobalt nanosheet catalyst for selective CO_2 conversion to ethanal, J. Am. Chem. Soc. 143 (2021) 15335–15343.

[105] S. Gao, Y. Lin, X.C. Jiao, Y.F. Sun, Q.Q. Luo, W.H. Zhang, D.Q. Li, J.L. Yang, Y. Xie, Partially oxidized atomic cobalt layers for carbon dioxide electroreduction to liquid fuel, Nature 529 (2016) 68–71.

[106] H.S. Jeon, I. Sinev, F. Scholten, N.J. Divins, I. Zegkinoglou, L. Pielsticker, B.R. Cuenya, Operando evolution of the structure and oxidation state of size-controlled Zn nanoparticles during CO_2 electroreduction, J. Am. Chem. Soc. 140 (2018) 9383–9386.

[107] D.H. Won, H. Shin, J. Koh, J. Chung, H.S. Lee, H. Kim, S.I. Woo, Highly efficient, selective, and stable CO_2 electroreduction on a hexagonal Zn catalyst, Angew. Chem. Int. Ed. 128 (2016) 9443–9446.

[108] M.G. Kibria, C.T. Dinh, A. Seifitokaldani, P. De Luna, T. Burdyny, R. Quintero-Bermudez, M.B. Ross, O.S. Bushuyev, F.P. García de Arquer, P.D. Yang, A surface reconstruction route to high productivity and selectivity in CO_2 electroreduction toward C_{2+} hydrocarbons, Adv. Mater. 30 (2018) 1804867.

[109] Y.J. Pang, T. Burdyny, C.T. Dinh, M.G. Kibria, J.Z. Fan, M. Liu, E.H. Sargent, D. Sinton, Joint tuning of nanostructured Cu-oxide morphology and local electrolyte programs high-rate CO_2 reduction to C_2H_4, Green Chem. 19 (2017) 4023–4030.

[110] M.C. Luo, Z.Y. Wang, Y.C. Li, J. Li, F.W. Li, Y.W. Lum, D.H. Nam, B. Chen, J. Wicks, A. Xu, Hydroxide promotes carbon dioxide electroreduction to ethanol on copper via tuning of adsorbed hydrogen, Nat. Commun. 10 (2019) 1–7.

[111] W.L. Fu, Z. Liu, T.Y. Wang, J.S. Liang, S. Duan, L.F. Xie, J.T. Han, Q. Li, Promoting C_{2+} production from electrochemical CO_2 reduction on shape-controlled cuprous

oxide nanocrystals with high-index facets, ACS Sustain. Chem. Eng. 8 (2020) 15223–15229.
[112] W. Luc, X.B. Fu, J.J. Shi, J.J. Lv, M. Jouny, B.H. Ko, Y.B. Xu, Q. Tu, X.B. Hu, J.S. Wu, Two-dimensional copper nanosheets for electrochemical reduction of carbon monoxide to acetate, Nat. Catal. 2 (2019) 423–430.
[113] Y.H. Wang, Z.Y. Wang, C.T. Dinh, J. Li, A. Ozden, M. Golam Kibria, A. Seifitokaldani, C.S. Tan, C.M. Gabardo, M.C. Luo, Catalyst synthesis under CO_2 electroreduction favours faceting and promotes renewable fuels electrosynthesis, Nat. Catal. 3 (2020) 98–106.
[114] W. Chen, E.D. Cubuk, M.M. Montemore, C. Reece, R.J. Madix, C.M. Friend, E. Kaxiras, A comparative ab initio study of anhydrous dehydrogenation of linear-chain alcohols on Cu (110), J. Phys. Chem. C 122 (2018) 7806–7815.
[115] M. Zhang, W.B. Wei, S.H. Zhou, D.D. Ma, A.H. Cao, X.T. Wu, Q.L. Zhu, Engineering a conductive network of atomically thin bismuthene with rich defects enables CO_2 reduction to formate with industry-compatible current densities and stability, Energy Environ. Sci. 14 (2021) 4998–5008.
[116] L. Fan, C. Xia, P. Zhu, Y.Y. Lu, H.T. Wang, Electrochemical CO_2 reduction to high-concentration pure formic acid solutions in an all-solid-state reactor, Nat. Commun. 11 (2020) 1–9.
[117] F.C. Lei, W. Liu, Y.F. Sun, J.Q. Xu, K.T. Liu, L. Liang, T. Yao, B.C. Pan, S.Q. Wei, Y. Xie, Metallic tin quantum sheets confined in graphene toward high-efficiency carbon dioxide electroreduction, Nat. Commun. 7 (2016) 1–8.
[118] Y.F. Jia, F. Li, K. Fan, L.C. Sun, Cu-based bimetallic electrocatalysts for CO_2 reduction, Adv. Powder Mater. 1 (2021) 100012.
[119] F. Cheng, X.X. Zhang, K.W. Mu, X. Ma, M.Y. Jiao, Z.H. Wang, P. Limpachanangkul, B. Chalermsinsuwan, Y. Gao, Y.H. Li, Recent progress of Sn-based derivative catalysts for electrochemical reduction of CO_2, Energy Technol. 9 (2021) 2000799.
[120] M.Y. Zu, L. Zhang, C.W. Wang, L.R. Zheng, H.G. Yang, Copper-modulated bismuth nanocrystals alter the formate formation pathway to achieve highly selective CO_2 electroreduction, J. Mater. Chem. A 6 (2018) 16804–16809.
[121] X.L. Zhang, X.H. Sun, S.X. Guo, A.M. Bond, J. Zhang, Formation of lattice-dislocated bismuth nanowires on copper foam for enhanced electrocatalytic CO_2 reduction at low overpotential, Energy Environ. Sci. 12 (2019) 1334–1340.
[122] Y.B. Ma, J.L. Yu, M.Z. Sun, B. Chen, X.C. Zhou, C.L. Ye, Z.Q. Guan, W.H. Guo, G. Wang, S.Y. Lu, D.S. Xia, Y.H. Wang, Z. He, L. Zheng, Q.B. Yun, L.Q. Wang, J.W. Zhou, P.Y. Lu, J.W. Yin, Y.F. Zhao, Z.B. Luo, L. Zhai, L.W. Liao, Z.L. Zhu, R.Q. Ye, Y. Chen, Y. Lu, S.B. Xi, B.L. Huang, C.S. Lee, Z.X. Fan, Confined growth of silver-copper Janus nanostructures with {100} facets for highly selective tandem electrocatalytic carbon dioxide reduction, Adv. Mater. 34 (2022) 2110607.
[123] J. Wang, J. Yu, M. Sun, L. Liao, Q. Zhang, L. Zhai, X. Zhou, L. Li, G. Wang, F. Meng, Surface molecular functionalization of unusual phase metal nanomaterials for highly efficient electrochemical carbon dioxide reduction under industry-relevant current density, Small 18 (2022) 2106766.
[124] L.H. Luo, M.L. Wang, Y. Cui, Z.Y. Chen, J.X. Wu, Y.L. Cao, J. Luo, Y.Z. Dai, W.X. Li, J. Bao, Surface iron species in palladium-iron intermetallic nanocrystals that promote and stabilize CO_2 methanation, Angew. Chem. Int. Ed. 132 (2020) 14542–14550.
[125] X. Zhang, Z.M. Luo, P. Yu, Y.Q. Cai, Y.H. Du, D.X. Wu, S. Gao, C.L. Tan, Z. Li, M.Q. Ren, T. Osipowicz, S.M. Chen, Z. Jiang, J. Li, Y. Huang, J. Yang, Y. Chen, C.Y. Ang, Y.L. Zhao, P. Wang, L. Song, X.J. Wu, Z. Liu, A. Borgna, H. Zhang, Lithiation-induced amorphization of $Pd_3P_2S_8$ for highly efficient hydrogen evolution, Nat. Catal. 1 (2018) 460–468.
[126] Y.W. Lum, J.E. Huang, Z.Y. Wang, M.C. Luo, D.H. Nam, W.R. Leow, B. Chen, J. Wicks, Y.C. Li, Y.H. Wang, C.T. Dinh, J. Li, T.T. Zhuang, F. Li, T.K. Sham, D. Sinton, E.H. Sargent, Tuning OH binding energy enables selective electrochemical oxidation of ethylene to ethylene glycol, Nat. Catal. 3 (2020) 14–22.
[127] L.C. Pardo Pérez, D. Teschner, E. Willinger, A. Guiet, M. Driess, P. Strasser, A. Fischer, In situ formed "$Sn_{1-X}In_X$@$In_{1-Y}Sn_YO_Z$ core@shell nanoparticles as electrocatalysts for CO_2 reduction to formate, Adv. Funct. Mater. 31 (2021) 2103601.
[128] D. Wakerley, S. Lamaison, F. Ozanam, N. Menguy, D. Mercier, P. Marcus, M. Fontecave, V. Mougel, Bio-inspired hydrophobicity promotes CO_2 reduction on a Cu surface, Nat. Mater. 18 (2019) 1222–1227.
[129] S. Zhang, P. Kang, S. Ubnoske, M.K. Brennaman, N. Song, R.L. House, J.T. Glass, T.J. Meyer, Polyethylenimine-enhanced electrocatalytic reduction of CO_2 to formate at nitrogen-doped carbon nanomaterials, J. Am. Chem. Soc. 136 (2014) 7845–7848.
[130] Z. Cao, D. Kim, D. Hong, Y. Yu, J. Xu, S. Lin, X. Wen, E.M. Nichols, K. Jeong, J.A. Reimer, A molecular surface functionalization approach to tuning nanoparticle electrocatalysts for carbon dioxide reduction, J. Am. Chem. Soc. 138 (2016) 8120–8125.
[131] Y.G. Yao, Z.N. Huang, P.F. Xie, S.D. Lacey, R.J. Jacob, H. Xie, F.J. Chen, A. Nie, T.C. Pu, M. Rehwoldt, Carbothermal shock synthesis of high-entropy-alloy nanoparticles, Science 359 (2018) 1489–1494.
[132] Y.G. Yao, Q. Dong, A. Brozena, J. Luo, J.W. Miao, M.F. Chi, C. Wang, I.G. Kevrekidis, Z.J. Ren, J. Greeley, High-entropy nanoparticles: synthesis-structure-property relationships and data-driven discovery, Science 376 (2022) eabn3103.
[133] Y. Zhu, T.R. Kuo, Y.H. Li, M.Y. Qi, G. Chen, J.L. Wang, Y.J. Xu, H.M. Chen, Emerging dynamic structure of electrocatalysts unveiled by in situ X-ray diffraction/absorption spectroscopy, Energy Environ. Sci. 14 (2021) 1928–1958.
[134] H. An, L. Wu, L.D. Mandemaker, S. Yang, J. de Ruiter, J.H. Wijten, J.C. Janssens, T. Hartman, W. van der Stam, B.M. Weckhuysen, Sub-second time-resolved surface-enhanced Raman spectroscopy reveals dynamic CO intermediates during electrochemical CO_2 reduction on copper, Angew. Chem. Int. Ed. 60 (2021) 16576–16584.
[135] Z. Sun, H. Yin, K. Liu, S. Cheng, G.K. Li, S. Kawi, H. Zhao, G. Jia, Z. Yin, Machine learning accelerated calculation and design of electrocatalysts for CO_2 reduction, SmartMat 3 (2022) 68–83.